Speckle Noise Reduction via Homomorphic Elliptical Threshold Rotations in the Complex Wavelet Domain

by

Edmund Hui-On Ng

A thesis
presented to the University of Waterloo
in fulfilment of the
thesis requirement for the degree of
Master of Applied Science
in
Electrical and Computer Engineering

Waterloo, Ontario, Canada, 2005

Author's Declaration

I hereby declare that I am the sole author of this thesis. This is a true copy of the thesis, including any required final revisions, as accepted by my examiners.

I understand that my thesis may be made electronically available to the public.

Edmund Hui-On Ng

Abstract

Many clinicians regard speckle noise as an undesirable artifact in ultrasound images masking the underlying pathology within a patient. Speckle noise is a random interference pattern formed by coherent radiation in a medium containing many sub-resolution scatterers. Speckle has a negative impact on ultrasound images as the texture does not reflect the local echogenicity of the underlying scatterers. Studies have shown that the presence of speckle noise can reduce a physician's ability to detect lesions by a factor of eight. Without speckle, small high-contrast targets, low contrast objects, and image texture can be deduced quite readily.

Speckle filtering of medical ultrasound images represents a critical pre-processing step, providing clinicians with enhanced diagnostic ability. Efficient speckle noise removal algorithms may also find applications in real time surgical guidance assemblies. However, it is vital that regions of interests are not compromised during speckle removal. This research pertains to the reduction of speckle noise in ultrasound images while attempting to retain clinical regions of interest.

Recently, the advance of wavelet theory has lead to many applications in noise reduction and compression. Upon investigation of these two divergent fields, it was found that the speckle noise tends to rotate an image's homomorphic complex-wavelet coefficients. This work proposes a new speckle reduction filter involving a counter-rotation of these complex-wavelet coefficients to mitigate the presence of speckle noise. Simulations suggest the proposed denoising technique offers superior visual quality, though its signal-to-mean-square-error ratio (S/MSE) is numerically comparable to adaptive frost and kuan filtering.

This research improves the quality of ultrasound medical images, leading to improved diagnosis for one of the most popular and cost effective imaging modalities used in clinical medicine.

Acknowledgments

In the course of completing my graduate degree, I have had the pleasure and privilege of working with some wonderful people, whom all deserve my gratitude.

In particular, my supervisor, Professor K. T. Wong provided support and guidance over the years and I would like to thank him for his diligent critique of my work. I would also like to thank Jerry Lam for his enthusiasm and his help in creating the user interface for the image simulations.

Finally and most importantly, I would like to thank my family for their constant love and encouragement. I did it!

This is dedicated to all the people I love.

Contents

List of Figures

List of Tables

Chapter 1

Introduction

Coherent imaging systems such as ultrasound suffer from speckled noise, creating images that appear inferior to those generated by other medical imaging modalities. Speckle is a random interference pattern formed by coherent radiation in a medium containing many sub-resolution scatterers. Speckle has a negative impact on ultrasound images as the texture does not reflect the local echogenicity of the underlying scatterers. The local brightness of the speckle pattern, however, does reflect the local echogenicity of the underlying scatterers. Clinically, speckle noise has been shown to reduce the ability to detect lesions by a factor of eight [1]. Without speckle, it may be possible to observe:

1. small differences in mean image brightness
2. small high-contrast targets
3. low contrast objects
4. changes in speckle-free image texture

Speckle filtering of medical ultrasound images represents a critical pre-processing step, providing clinicians with enhanced diagnostic ability. Efficient speckle noise removal algorithms may also find applications in real time surgical guidance assemblies. However, it is vital that regions of interests are not compromised during speckle removal. This chapter details the construction of an ultrasound image and details the speckle reduction problem investigated in this thesis.

1.1 An Overview of Ultrasound Imaging

Ultrasound has become one of the most popular modalities in clinical imaging and is particularly important in developing countries. It has found application in monitoring unborn foetus, the cardiovascular system, gynecology, abdomen, thyroid, and the other parts of the body [2]. Recently, ultrasound systems have found increasing use in surgical and intravascular applications as a guide for interventional procedures [3]. The popularity of ultrasound can be attributed to two factors:

- Of all the imaging modalities currently used in the medical field for diagnostic purposes, ultrasound systems are considered to pose the least risk to the patient. This is because non-audible sound waves with frequencies above 20 kHz are not known to cause any adverse biological effects in humans [4]. Contrasting this with other imaging methods like CT, which may expose the patient to potentially harmful doses of radiation, ultrasound represents a non-invasive, minimal risk strategy to view the internal systems of the human body.

- Another advantage to ultrasound systems is the simple technology employed, making ultrasound scanners comparably less expensive and more portable

than other imaging equipment.

Ultrasound scanners today are based on echo imaging technology [5]. A high frequency pulse of acoustic energy is emitted into the patient by a transducer. This energy interacts with the patient's blood and tissues and a portion of the transmitted energy returns to the transducer to be detected. From this data, it is possible to derive two properties concerning the nature of the medium:

1. The distance from the transducer which the interaction occurred can be gaged if the initial propagation velocity is known.

2. Reflection at tissue boundaries causes a different amount of return energy (amplitude and phase) due to different tissue characteristic impedance, providing a property used to distinguish different mediums.

Based on the time delay and intensity of reflected pulses, an image indicating tissue interfaces can be constructed. While many modes of image acquisition exists (including "motion mode" or M mode, Continuous Wave Mode, Spectral Doppler, Color Doppler and 3D-Mode), this thesis is concerned with ultrasound systems which produce B-mode or "brightness mode" images. B-mode images are grey scale representations of the underlying physiology. A typical image is show in figure 1.1.

The longitudinal compression waves generated by the ultrasonic transducer interacts with the tissue and blood. The wave energy may be absorbed, reflected, or scattered. Some of the reflected and scattered energy is detected by the transducer and the information derived from the received data may be used to form an image. The image formation process is due to three main factors: the velocity of the wave

[1]curtesy of GE http://www.gehealthcare.com/worldwide.html

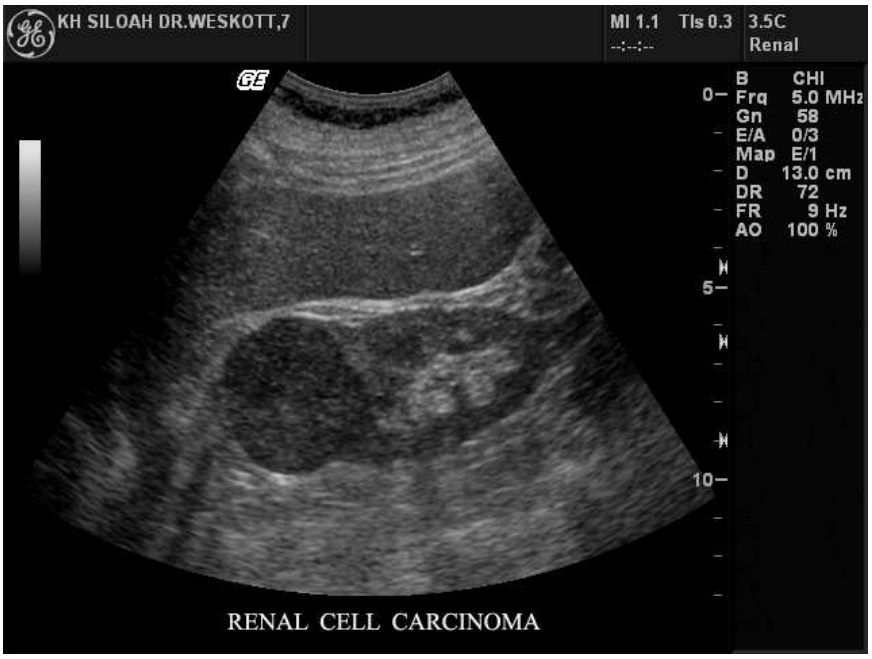

Figure 1.1: Typical B-mode Ultrasound Image[1]

in the tissue, the attenuation the acoustic wave experiences, and the noise present in the return signal. Acoustic waves propagate through a medium with a characteristic velocity. It has been clinically accepted that acoustic waves travel through soft tissue at a mean speed of 1540 m/sec with a 6% variation (due to different mediums) under standard temperature and pressure [4]. The speed of sound in a medium is given by equation 1.1.

$$c = \sqrt{\frac{K}{p_0}} \tag{1.1}$$

where K is the bulk elastic modulus and p_0 is the tissue density. The variation is due to changes in elasticity. Acoustic energy attenuates as the wave travels deeper into the body since the wave is continuously absorbed, reflected, or scattered.

This attenuation occurs mainly through reflection and scattering [6] and is often modelled as an exponential function of distance as shown in equation 1.2.

$$S(x) = S_0 e^{-\alpha x} \tag{1.2}$$

where S is the signal amplitude, S_0 is a constant, and α is the attenuation coefficient. In general, tissue intensity is reduced by half every 0.8 cm using an acoustic wave of 5 MHz [4].

The received return signal is also based on the reflection and scattering from the medium. These reflections are due to the difference in acoustic impedance (larger than the wavelength) across tissue interfaces. The characteristic acoustic impedance is given by equation 1.3.

$$Z = p_0 c = \sqrt{p_0 K} \tag{1.3}$$

where c is the speed of sound and p_0 is the tissue density as before. Acoustic impedance has units of pressure per unit velocity and works similar to electromagnetic waves in transmission lines. An acoustic wave travelling from a medium with impedance Z_1 to a medium with medium Z_2 will have part of the wave reflected and part of the wave transmitted. The reflection coefficient is given by equation 1.4.

$$\Gamma = \left(\frac{Z_2 - Z_1}{Z_2 + Z_1} \right)^2 \tag{1.4}$$

Notice that if the incident wave is not normal to the interface, the transmitted wave will be refracted according to Snell's law. Notice that the strength of the signal returned to the transducer will be orientation dependent. Typical acoustic values found in clinical settings for various media are summarized in table 1.1.

Table 1.1: Acoustic Properties for Different Media[4]

Medium	**Speed of Sound** (m/s)	**Impedance** $\left(\frac{10^6 kg}{m^2 s}\right)$	**Attenuation** (dB/cm at 1 MHz)
Air	344	0.0004	12.0
Water	1480	1.48	0.0025
Fat	1410	1.38	0.63
Muscle	1566	1.70	1.3 - 3.3
Liver	1540	1.65	0.94
Bone	4080	7.80	20.0

Note that if the interaction is between a tissue structure of comparable or smaller size than the acoustic wavelength, scattering will occur [7]. These small structures reflect waves in all directions (Rayleigh Scattering). A volume of scatterers (eg: blood cells or tissue) give rise to the speckle pattern seen in ultrasound. Notice that the component of the return signal due to scattering may or may not depend on orientation. For instance, the striations in muscles cells make orientation important while liver cells have no orientational dependency.

A simplified block diagram of a typical ultrasound scanning system is shown in figure 1.2.

The pulser generates the electromagnetic waves sent to the transducer. The center frequency, shape, duration, and amplitude of the pulser signal determines the intensity and spectral content of the acoustic signal. A center frequency of 2 to 10 MHz is commonly used. The wave shape may be monopolar squares or of arbitrary complexity. The duration may be boardband or narrowband depending on application and amplitudes range from 2 to 200 volts.

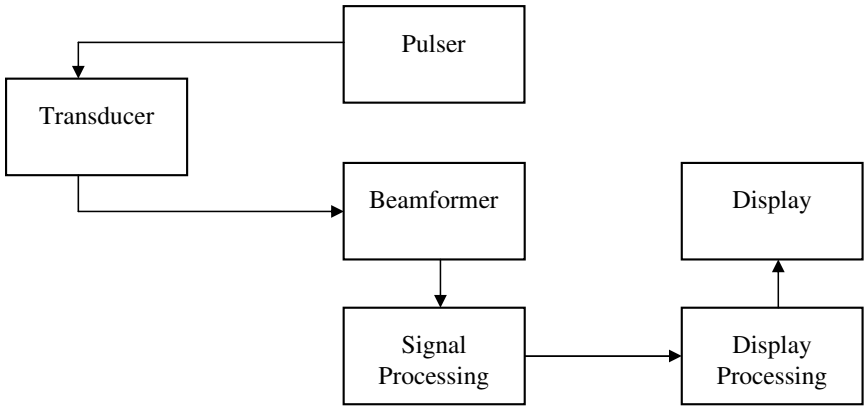

Figure 1.2: Block Diagram of an Ultrasound Scanner[4]

Central to any ultrasound imaging system is the transducer, a device that converts electrical signals to and from sound waves. Ultrasound transducers have piezoelectric crystals in contact with tissues using an index matching gel. As the transducer is moved (either mechanically or manually) over the surface of the skin, a 2D image is produced. Different configurations for transducer elements exist including single piston, annular array, linear array, and etc. Each type of transducer can be used in a variety of examinations and offer different tradeoffs with respect to simplicity, resolution, mechanical interfacing and focus.

Note that the array configuration in the transducer provides the ability to steer and focus the acoustic beam. In transmit mode, a focal point is chosen for a burst while continuous focusing is performed under a receive mode. In general, a time multiplex technique is used as frequency domain beamforming have not received widespread acceptance. As no beamforming technique is currently ideal, a particular pixel image often represents a spatially weighted volume rather than a point in space. Contributions from outside the main lobe creates side lobe artifacts.

The composite beamformed signal is subjected to a variety of signal processing operations before it is presented to the display system. To produce a B-scan image, the composite signal is filtered, log-compressed and multirate filtering is employed to match the display resolution. As the precise order of filtering and filter design determines the quality of the final image, this information is kept proprietary by manufacturers.

The display processing and display system provides colour and grey scale mapping for image formatting. Data collected is shown in a CRT or equivalent system. Additional information on the physics and instrumentation of ultrasound machines are discussed in [5].

1.2 Problem Formulation

A review of the ultrasound image construction process sets the stage for proposing additional signal processing strategies post image formation. Initially, this thesis reviews and investigates the theoretical and empirical effects of the first and second order properties of speckle noise. An attempt is made to analyze and characterize the noise variance from the wavelet coefficients in relation to the wavelet decomposition level.

Standard speckle reduction algorithms and filters are subsequently investigated. In addition, the development of a new class of speckle noise reduction filter is introduced using the complex wavelet transform and different wavelet thresholding techniques. Both the symmetric Daubechies and the dual tree wavelet formulations will be discussed and characterized. The aim is to achieve optimal speckle removal while retaining relevant clinical information. A thorough comparison between the

new proposed algorithm and the standard reduction algorithms is made through simulations under various speckle noise metrics.

In conclusion, applications of the speckle reduction algorithm to medical imaging algorithms in cardiac motion estimation is discussed and simulations are performed to gauge the effectiveness of the proposed noise reduction technique in cardiac motion estimation algorithms.

Chapter 2

Speckle Noise

Speckle noise is the characteristic effect seen in ultrasound images that contribute to the visual noise. The image of a relatively uniform object with many scattering sources within a resolution cell will have pixel values that vary randomly with position due to constructive and destructive interference.

2.1 Speckle Noise Statistics

Several models have been proposed that explain the mechanism of speckle noise in ultrasound. The rough volume model identifies a region of the object (referred to as a the resolution cell) where the scattering structures are too fine to be resolved. The scattering waves within the resolution cell may destructively interfere, producing no noise, or constructively interfere, producing high echo noise. This phenomenon is further complicated by high side or grating lobe levels in the transducer, inhomogeneous propagation medium, or multiple scattering paths [3]. Theoretically, the typical speckle size and shape is the same as the resolution cell. However, the

speckle size and shape may vary as a result of diffraction fields and frequency dependent attenuation in the transducer. Furthermore, phase cancellations generate finer speckle patterns so the resolution cell size is not represented by the shape and size of the speckle noise in the image.

Coherent imaging processes employed by synthetic aperture radar (SAR) and narrow-band ultrasound suffer from speckle noise. Speckle is caused by constructive and destructive interference of coherent waves reflected by the many elementary scatterers contained within the imaged resolution cell. For distributed targets, the signal received by the transceiver is a superposition of many small reflections. Under the assumption that in each resolution cell:

- no single scatterer dominates over all others combined;
- the number of scatterers is large and scatterers are statistically identical and independent; and
- the maximum range extent of the target is many wavelengths across, as a consequence of which, scatterers contribute very different phases,

The vector sum of the backscattered electric field is equivalent to a two-dimensional (2-D) random walk process with independently and identically Gaussian distributed real and imaginary components [8].

The presence of speckle bears no relationship to the tissue structure. Note however, if the object contains some resolved structure or some underlying regular distribution of scatterers, the image texture may not be a function of only the imaging system and may be used to classify the structure. The pattern of speckle is determined entirely by the physical scattering process as the results are completely repeatable if nothing moves or changes. (This is highly unlikely).

2.2 Speckle Noise Formation in Ultrasound

The nature of the speckle pattern can be categorized into one of three classes according to the number of scatterers per resolution cell or the so called scatterer number density (SND), in addition to their spatial distribution and the characteristics of the imaging system itself. These classes are:

- The FFS pattern occurs when many fine randomly distributed scattering sites exist within the resolution cell of the pulse-echo system. In this case, the amplitude of the backscattered signal can be modelled as a Rayleigh distributed random variable with a constant SNR of 1.92 [9]. Under such conditions, the textural features of the speckle pattern represent a multivariate signature of the imaging instrument and its point spread function [1]. Blood cells are typical examples of this type of scatterers.

- Nonrandomly distributed with long-range order (NRLR) [10]. Examples of this type are the lobules in liver parenchyma. It contributes a coherent or specular backscattered intensity that is in itself spatially varying. Due to the correlation between scatterers, the effective number of scatterers is finite . This situation can be modeled by the K-distribution. This type is associated with SNR below 1.92 [11]. It can also be modeled by the Nakagami distribution [1].

- Nonrandomly distributed with short-range order (NRSR) [11]. Examples of this type include organ surfaces and blood vessels. When a spatially invariant coherent structure is present within the random scatterer region, the probability density function (PDF) of the backscattered signals becomes close to the Rician distribution. This class is associated with SNR above 1.92 [12].

Hence, the coherence phenomena make the SNR an ambiguous feature that cannot be used alone to characterize the speckle model. The deviation in image properties due to the presence of coherent structures that are partially or completely resolved results in a speckle pattern that is no longer entirely characteristic of the imaging system [9]. It should, therefore, be possible to use these deviations to classify each local region of the image according to how much it resembles the FFS normally generated by that particular imaging system in that part of the image. This measure of similarity can then be used to control the spatial bandwidth of a smoothing filter of some kind so that regions within the image that closely resemble the FFS are replaced by a local mean value. At the other extreme, regions with properties that are least similar to FFS should be kept unaltered [9].

2.3 Mathematical Formulation of Speckle

In general, the nature of speckle noise patterns in ultrasound images can be described statistically as a random walk process. The behaviour of a fully developed speckle is similar to that of a Brownian motion. The in-phase component, A_R and the quadrature component, A_I of the speckle amplitude A can be described by statistically independent random variables of Gaussian distributions with zero mean and identical variances. The circularly Gaussian distribution is shown in equation 2.1.

$$A = A_R + jA_I \tag{2.1}$$

The intensity of the speckle $u = A_R^2 + A_I^2$ has a negative exponential distribution given by equation 2.2

$$p(u) = \frac{1}{\bar{u}} e^{\frac{u}{\bar{u}}} \tag{2.2}$$

where P is the mean of the intensity U . In practice, a digital image echo returns is represented by spatial variations of pixel intensities over the scene. Systems where a large number of scatterers exist develop full speckle characteristics similar to random multiplicative noise which follows the multiplicative model. In this representation, a multiplicative speckle model with an exponential distribution is assumed and can be written as equation 2.3

$$I(t) = R(t)u(t) \tag{2.3}$$

where $t = (x, y)$ represents the spatial coordinates of the image, $I(t)$ is the observed image intensity at $t = (x, y)$. $R(t)$ denotes the corresponding reflectivity or backscattering coefficient. and $u(t)$ is a multiplicative speckle noise statistically independent of $R(t)$, with unit mean Z and unit variance σ_u^2. This model formulates the speckle as a multiplicative modulation of the scene reflectivity. Hence, the speckle effects are more pronounced in a high intensity area than in a low intensity area.

When the image is processed linearly, the shape of its gray-level normalized probability density function (as related to C) is a discrete Rayleigh distribution as described in equation 2.4 with unit mean and variance $(4/\pi - 1)$. [3]

$$u(t) = \frac{\pi t}{2} \exp\left(-\frac{\pi t^2}{4}\right) \tag{2.4}$$

To take advantage of additive noise reduction methods, a logarithmic transformation is often applied to a speckled image. This transform converts equation 2.3

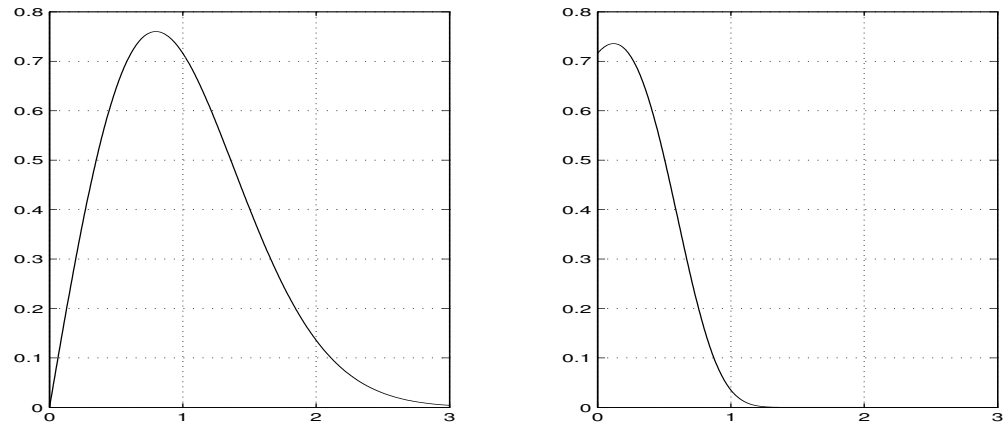

Figure 2.1: The Rayleigh Distribution (left) and The Log Rayleigh Distribution (right)

into:

$$\hat{I(t)} \quad = \quad \log R(t)u(t) = \log R(t) + \log u(t) = \hat{R}(t) + \hat{u}(t) \tag{2.5}$$

After this transformation, the pdf $\hat{u}(t)$ becomes equation 2.6 as described in [8].

$$\hat{u}(t) \quad = \quad \frac{\pi e^{2t}}{2} \exp\left(-\frac{\pi e^{2t}}{4}\right) \tag{2.6}$$

The second-order statistical classification of speckle relates to the coarseness of the spatial structure to the image granularity. The autocorrelation function of a scattering field as applied to lasers was derived by Goodman and can be applied in this case [13]. Factors such as the sensor's resolution element, and thermal noise also attribute to this correlation in ultrasound images. Although it is out of the scope of this paper to discuss all correlation sources, a simple theoretical model based on the previous discussion will be utilized to study the impact of speckle noise in the complex wavelet domain. The overall correlation properties are estimated by

measuring the normalized autocovariance function of a sample image.

In subsequent analysis, the dependence of the scene and image on t is dropped for simplicity of dicussion.

2.4 Metrics for Quantifying Speckle Noise

2.4.1 Signal to Mean Square Noise Ratio

One way of measuring the effect of speckle noise is to calculate the signal-to-noise ratio (SNR). The SNR can be measured by computing the mean signal intensity over a certain region of interest (ROI) and dividing this by the standard deviation of the signal from a region outside the image.

However, the noise is not always uniformly distributed over the image as in the case of ultrasound images. As a consequence, other methods may be a more accurate measure of image quality and speckle removal efficiency.

2.4.2 Peak Signal to Noise Ratio

Peak signal to noise ratio (PSNR) is used to measure the difference between two images. It is defined as equation 2.7

$$PSNR = 20 \times \log\left(\frac{b}{rms}\right) \tag{2.7}$$

where b is the largest possible value of the signal (typically 255 or 1), and rms is the root mean square difference between two images. The PSNR is given in decibel

units (dB), which measure the ratio of the peak signal and the difference between two images. An increase of 20 dB corresponds to a ten-fold decrease in the rms difference between two images.

2.4.3 Equivalent Number of Looks

Another good approach of estimating the speckle noise level in a SAR image is to measure the equivalent numbers of looks (ENL) over a uniform image region. The ratio of the standard deivation to the mean in the homogeneous areas of an image is a good measure of speckle strength. This ratio is often used to measure the performance of speckle reduction. The speckle index β is calculated according to equation 2.8

$$\beta = \frac{\sqrt{x_{\sigma^2}}}{x_\mu} \tag{2.8}$$

where x_μ and x_{σ^2} is the mean and variance of the image.

From the speckle index, the equivalent number of looks (ENL) is defined by equation 2.9 [14]. The ENL is a measure of the smoothness of the image.

$$ENL = \frac{1}{\beta^2} \tag{2.9}$$

Large ENL values generally corresponds to a better quantitative noise reduction performance. However, the ENL value also depends on the size of the tested region. Theoretically, a large region will almost always produce higher ENL value than

smaller regions. Due to the difficulty in identifying uniform areas in the image, the image is segmented into smaller areas of 25 $\times$ 25 pixels. Each region is then used to calculate the ENL value and these smaller areas are averaged to obtain the final ENL values.

2.4.4 Human Visual System Model

Because of the complex response of the human visual system, typical measurements of image system quality such as the detective quantum efficiency, mean transfer function, and signal-to-noise ratio cannot always be used to determine conditions for optimal perceptual image quality. However, due to the implementation complexities, the HVS models presented for image analysis will not be included in this thesis.

2.5 Summary

In this chapter, we discussed the causes of speckle noise in ultrasound and the various mathematical models associated with the formulation of the speckle noise pattern. The various noise content metrics were also discussed. In the next chapter, the standard filters currently used to mitigate the speckle noise in images is investigated.

Chapter 3

Standard Speckle Filters

Many types of speckle reduction techniques have been developed over the years to reduce noisy images captured in coherent systems such as synthetic aperture radar (SAR) and ultrasonic imagery. This chapter investigates the standard methodologies used in the reduction of speckle noise.

Speckle suppression techniques can be classified into two categories [14]. The first strategy referred to as multi-look processing is to average several looks obtained from the same scene. This process is equivalent to applying a lowpass (LP) filter to the images. Using an LP filter by averaging the multi-look scenes is an effective and simple strategy when the areas of interest on the image are mostly homogeneous. Unfortunately, most applications are required to deal with features that contain high frequency information (textures and edges). With these images, the use of LP filters usually results in poor performance, since it suppresses both the speckle and the texture information at the same time [15].

The second category is to smooth the speckle after images have been formed. Many speckle reduction filters which are adaptive to the local texture information

are proposed. These adaptive filters can smooth speckle in homogeneous areas while preserving texture and high frequency information in heterogeneous areas . In the past few years, numerous adaptive filters have been proposed. Among the best known are the Lee [14], the Kuan [16, 17], the Frost [18], and the modified Lee and modified Frost filters [19]. More recently, speckle filters based on the Maximum A Posteriori (MAP) probability [19] and wavelets have been proposed. These filters have achieved a degree of suppressing speckle while preserving the texture information. Each speckle reduction filter is designed based on different criteria and parameters. These filters represent unique tradeoffs between noise reduction, imaging smoothing, computational complexity, and visual representation. Ultimately, the goal of speckle reduction is to smooth out the image while preserving textural information and structural features, such as edges.

In the following sections, the standard speckle filters include the Median Filter, Statistic Lee Filter, Kuan filter, Frost filter, and the Gamma/MAP filter is discussed. The wavelet filter is briefly introduced and developed in subsequent chapters. An enhancement of the traditional wavelet filter is proposed in this thesis.

3.1 Median Filter

The median filter performs spatial filtering in a square-moving window known as the kernel. This filtering is based on the statistical relationship between the central pixel and the surrounding pixels.[1] Usually, a larger filter window implies greater smoothing and higher computational complexity. Generally, a 3x3 window or 7x7 window yields the best results. Figure 3.1 shows an example of the 5x5 median

[1] An odd number is used as the dimension for the square window.

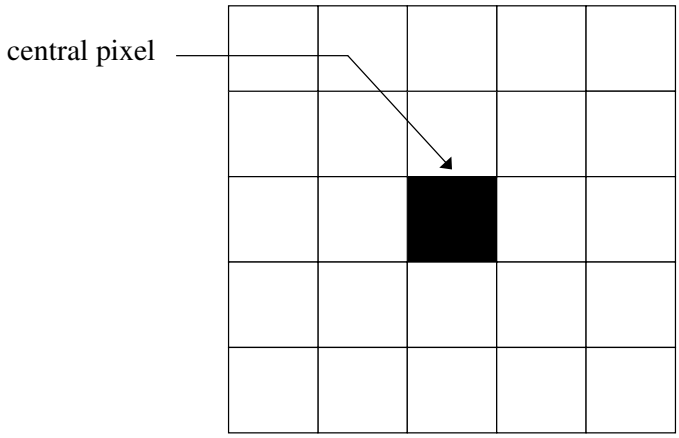

Figure 3.1: A 5x5 Median Sliding Window

filter spatial kernel.

The median filter is based on local statistical data given in the filter window. This data is used to determine the noise variance within the central pixel. The surrounding pixels are sorted into an order set and the center pixel is replaced with the median value. This filter is non-linear in nature and works well with impulse noise while retaining sharp edges in the image. More extensive investigation into the median filter along with various variations in its implementations can be found in [14].

3.2 Statistic Lee Filter

The Lee filter is based on a linear speckle noise model and a minimum mean square error (MMSE) design approach. The lee filter identifies regions with low and constant variance as areas for noise reduction.

In a region with no signal activity, the filter outputs the local mean. When

signal activity is detected, the filter passes the original signal through unchanged. This is achieved by implementing a filter of the form specified by equation 3.1.

$$\hat{R} = WI_t + (1 - W)\bar{I} \tag{3.1}$$

where I_t is the central pixel in the t^{th} window and W is the weighting function ranging between 0 for flat regions to 1 for regions with high signal activity. The weighting function is calculated according to equation 3.2

$$W = 1 - \frac{C_u^2}{C_I^2} \tag{3.2}$$

where $C_u = \frac{\sigma_u}{\bar{u}}$ and $C_I = \frac{\sigma_I}{\bar{I}}$ are the coefficient of variation of the noise u and the image I.

In area's of high variance, edges are assumed and little to no noise smoothing is done. In other words, the Lee filter smoothes away noise in flat regions, but leaves fine details unchanged. Therefore, its major drawback is that it leaves noise in the vicinity of edges and lines.

The mean and standard deviation are calculated from local regions in the image defined by smaller windows generally with dimensions 3×3,5×5 or 7×7. Within each window, the local mean and variance are estimated according to equation 3.3.

$$\begin{aligned} \bar{I} &= \tfrac{1}{N} \textstyle\sum_{i=1}^{N} t_i \\ \sigma_I^2 &= \tfrac{1}{N-1} \textstyle\sum_{i=1}^{N} (t_i - \bar{t})^2 \end{aligned} \tag{3.3}$$

where N is the number of pixel in the local window, $\bar{I}$ is the mean pixel intensity, σ_I^2 is the variance of the pixel intensity.

3.3 Kuan Filter

In the Kuan Filter [16], the multiplicative noise model is first transformed into a signal-dependent additive noise model. Then the MMSE criterion is then applied to this model. The resulting filter has the same form as the Lee filter but with a different weighting function as shown in equation 3.4

$$W = \frac{1 - \frac{C_u^2}{C_I^2}}{1 + C_u^2} \tag{3.4}$$

The Kuan filter made no approximation to the original model. From this point of view, it can be considered to be superior to the Lee filter. The Kuan filter can be derived directly by applying the MMSE criterion to the multiplicative model.

3.4 Enhance Frost Filter

The Frost filter differs from the Lee and Kuan filters with respect that the scene reflectivity $\hat{R}$ is estimated by convolving the observed image with the impulse response of the coherent imaging system. The system's impulse response is calculated by minimizing the mean square error between the observed image and the scene reflectivity model, assumed to be an autoregressive process. The resulting filter after some simplifications can be written like equation 3.5.

$$\hat{I}_t = \exp\left(-KC_I^2|t|\right) \tag{3.5}$$

where K is a constant controlling the damping rate of the impulse response function at the pixel to be filtered. When the variation coefficient C_I^2 is small, the filter

behaves like an LP filter smoothing out the speckles; when C_I^2 is large, it has a tendency to preserve the original observed image.

To improve upon the frost filter, Lopes et al. [19] propose to divide an image into areas belonging to one of three classes:

- Homogeneous areas in which the speckles may be eliminated simply by applying an LP filter
- Heterogeneous areas in which the speckles are to be reduced while preserving texture
- areas containing isolated point targets, where the filter should preserve the observed value.

Areas are classified based on the variation coefficients, C_u and C_I . Lopes et al. modified Frost (equation 3.6, 3.7) filters using this classification.

$$m(t) = \exp\left(-K\,\mathrm{func}(C_I(t_0))|t|\right) \tag{3.6}$$

where $\mathrm{func}(C_I(t_0))$ is a hyperbolic function of $C_I(t_0)$ defined as follows

$$\mathrm{func}(C_I) = \begin{cases} 0, & \text{for } C_I(t_0) < C_u \\ \frac{C_I(t_0)-C_u}{C_{max}-C_I(t_0)}, & \text{for } C_u \le C_I(t_0) \le C_{max} \\ \infty, & \text{for } C_I(t_0) > C_{max} \end{cases} \tag{3.7}$$

A modified Lee filter may also be derived in this manner. Comparing the modified filters with the original, it can be seen that at the two extremes (i.e. the homogeneous area class and isolated point target class), the output is forced to be

equal to the averaged value and the observed value without filtering, respectively. Between these two extremes is the heterogeneous class. In this class, the modified filters have the similar forms as the original ones, but the filter responses are "exaggerated" by introducing a hyperbolic function to satisfy the requirement that "the more heterogeneous the area is, the less it has to be smoothed" [19].

3.5 Gamma/MAP Filter

Applying the maximum a posteriori (MAP) approach to speckle proposed by Kuan et al. [17], the a priori knowledge of the probability density function (pdf) of the scene is required. The scene reflectivity was assumed to be Gaussian distributed (although this is not quite realistic since it implicitly assumes a negative reflectivity) although a gamma distribution is also used [19]. The Kuan MAP filter requires specification of two thresholds as given by equation 3.8.

$$\hat{R}(t_0) = \begin{cases} \bar{I}(t_0), & \text{for } C_I(t_0) < C_u \\ \frac{(\alpha-L-1)\bar{I}(t_0)+\sqrt{\bar{I}^2(t_0)(\alpha-L-1)^2+4\alpha L\bar{I}(t_0)}}{2\alpha}, & \text{for } C_u \leq C_I(t_0) \leq C_{max} \\ I(t_0), & \text{for } C_I(t_0) > C_{max} \end{cases} \tag{3.8}$$

where L is the number of looks, $C_{max}(t_0) = \sqrt{2}C_u$, and $\alpha = \frac{1+C_u^2}{C_I^2(t_0)-C_u^2}$

3.6 Wavelet Filter

As a denoising method, wavelet shrinkage, often referred to as hard/soft thresholding, is well known; wavelet shrinkage is based on a policy of thresholding wavelet coefficients toward zero in each wavelet domain. In this thesis, we have proposed several alternative approaches that reduce or compress the amplitude of wavelet coefficients, and we have successfully applied it to ultrasound images and speckle noised data. In the next chapter, we discuss the mathematical formulation of wavelets and the newly developed complex wavelet basis to set up the noise reduction algorithm presented in chapter 5.

Chapter 4

Wavelet Theory in the Complex Domain

The wavelet transform has been extensively studied in the past decade as a tool for imaging processing and has found a unique application in compression and noise reduction. The foundation of this research in based on signal analysis in both the time and frequency domain simultaneously. Not only does the wavelet transform dissect signals into their component frequencies, they also vary the scale at which the component frequencies are analyzed. Therefore wavelets, as component pieces used to analyze a signal, are limited in space.

4.1 Fundamental Equation of Wavelet Theory

The dilation equation (two-scale, refinement equation) also known as the wavelet equation is central to wavelet theory [2].

$$\begin{aligned} \exists h \in l_2(\mathbb{Z}): \quad \varphi(x) &= \sqrt{2}\sum_{k\in\mathbb{Z}} h_k \varphi(2x-k) \\ \exists g \in l_2(\mathbb{Z}): \quad \psi(x) &= \sqrt{2}\sum_{k\in\mathbb{Z}} g_k \varphi(2x-k) \end{aligned} \tag{4.1}$$

This is an equation relating the mother wavelet (father function) to the scaling function at the next finer scale. All these basis functions are generated from a single function, called the mother wavelet, by dilation and translation. Clearly different choices for the the mother wavelet yield different wavelet bases [20].

Suppose we would like to decompose a signal (in a scaling function basis at a given scale) into detail coefficients and scaling coefficients at the next, coarser scale (equation 4.2).

$$\begin{aligned} f_{j+1}(x) &= \sum_{k\in\mathbb{Z}} s_{j+1,k}\varphi_{j+1,k}(x) \\ &\text{decomposes to} \\ f_{j+1}(x) &= \sum_{k\in\mathbb{Z}} s_{j,k}\varphi_{j,k}(x) + \sum_{k\in\mathbb{Z}} w_{j,k}\phi_{j,k}(x) \end{aligned} \tag{4.2}$$

Finding $s_{j,k}$ and $w_{j,k}$ from $s_{j+1,k}$ is considered a forward wavelet transform (equation 4.3) [21].

$$\begin{aligned} w_{j,k} &= \left\langle f_{j+1}, \tilde{\psi}_{j,k} \right\rangle \\ &= \left\langle f_{j+1}, \sum_{k\in\mathbb{Z}} \tilde{g}_l \tilde{\varphi}_{j+1,2k+l} \right\rangle \\ &= \sum_{l\in\mathbb{Z}} \tilde{g}_{l-2k} s_{j+1,l} \\ s_{j,k} &= < f_{j+1}, \tilde{\varphi}_{j,k} > \\ &= \sum_{l\in\mathbb{Z}} \tilde{h}_{l-2k} s_{j+1,l} \end{aligned} \tag{4.3}$$

The inverse is also easy to find using the wavelet equation (equation 4.4):

$$\begin{aligned}\sum_{l\in\mathbb{Z}} s_{j+1,l}\varphi_{j+1,l} &= \sum_{k\in\mathbb{Z}} s_{j,k}\varphi_{j,k} + \sum_{k\in\mathbb{Z}} w_{j,k}\psi_{j,k} \\ &= \sum_{k\in\mathbb{Z}} s_{j,k} \sum_{l\in\mathbb{Z}} h_l\varphi_{j+1,2k+l} + \sum_{k\in\mathbb{Z}} w_{j,k} \sum_{l\in\mathbb{Z}} g_l\varphi_{j+1,2k+l} \\ &= \sum_{l\in\mathbb{Z}} \varphi_{j+1,l} \left(\sum_{k\in\mathbb{Z}} h_{l-2k}s_{j,k} + \sum_{k\in\mathbb{Z}} g_{l-2k}w_{j,k} \right)\end{aligned} \tag{4.4}$$

Therefore, we have equation 4.5

$$s_{j+1,l} = \sum_{k\in\mathbb{Z}} h_{l-2k}s_{j,k} + \sum_{k\in\mathbb{Z}} g_{l-2k}w_{j,k} \tag{4.5}$$

The forward and inverse transform may be considered as convolution sums [22]. However, the coefficients are upsampled in the reconstruction and downsampled in the decomposition due to the sum over 2k. This configuration is referred to as a filter bank and is shown in figure 4.1 [23].

4.2 Properties of Wavelet Transformation

Noise reduction using wavelet theory is based on three important concepts: sparsity, locality, and multiresolution [22].

4.2.1 Sparsity

Sparsity is a common characteristic of all wavelet transforms, which are said to have a decorrelating property. In essence, only a few coefficients are significant and

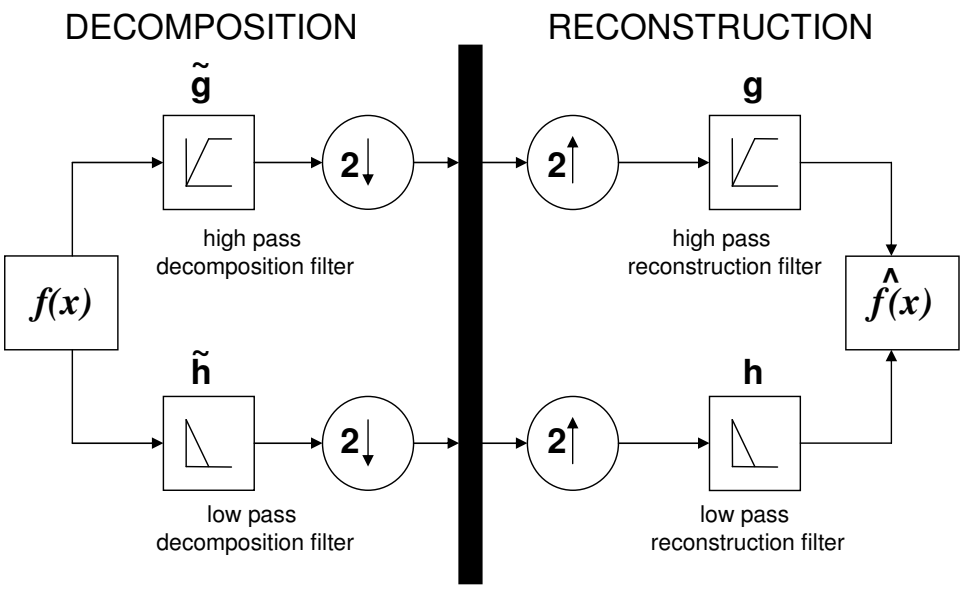

Figure 4.1: A one step wavelet decomposition followed by its reconstruction. This is a filter bank as the input is filtered and downsampled to get a low pass signal and a high pass signal. Reconstruction starts with upsampling by introducing zeros between every pair of points in LP and HP.

indicate singularities in the input.

To create a really sparse representation, the coefficients that lie between points of singularities should be as small as possible. The regions of relatively smooth behaviour should be well approximated by a polynomial.

4.2.2 Locality

Wavelet basis functions are short waves localized in time and space. This attribute contributes to much of the success wave analysis has in noise reduction applications. As each basis function also represents a scaled version of one mother function, each basis function can be identified by a unique combination of position and scale.

A wavelet coefficient details how much of the wavelet basis function is present in the total signal. A high coefficient means that the location and scale is an important contribution to a signal singularity. It says how far the signal is (in space) and the frequency (inverse of scale) or how large the signal ranges.

A intensity representation gives no direct scale information, as one pixel value gives no information regarding the neighbouring pixels. On the other hand, Fourier transforms using pure waves provides relative information regarding signals but destroys all time and space information. This is simply because a coefficient with a never ending wave cannot provide information regarding the location of one singularity. Although no basis function can give both time/space and frequency information precisely, the trade off between frequency uncertainty and time uncertainty can be minimized according to Heisenberg's uncertainty principle (equation 4.6).

$$\Delta x_{\psi} \Delta w_{\Psi} \quad \geq \quad \tfrac{1}{2} \tag{4.6}$$

where Δx_ψ and Δw_Ψ represent the uncertainty in space and frequency respectively. Wavelet coeffients operate at at this minimal threshold to provide local information in both time and frequency.

4.2.3 Multiresolution

Decomposing an image or function into a wavelet basis is an example of multiresolution analysis. Formally, multiresolution is defined in equation 4.7.

A sequence of nested closed subspaces $V_j \subset L_2[0,1], j = L, \ldots, J$ is called a multiresolution analysis (MRA) if

$$\begin{aligned}
\forall j \in \mathbb{Z}: \quad & V_j \subset V_{j+1} \\
& \lim_{j \to \infty} = \bigcup_{j \in \mathbb{Z}} V_j = L_2[0,1] \\
& \lim_{j \to -\infty} = \bigcap_{j \in \mathbb{Z}} V_j = 0 \\
& f(x) \in V_j \Leftrightarrow f(2x) \in V_{j+1}, j \in \mathbb{Z} \text{ (scale invariance)} \\
& f(x) \in V_0 \Leftrightarrow f(x+k) \in V_0, k \in \mathbb{Z} \text{ (shift invariance)} \\
& \exists \varphi(x) \in V_0 : \{\varphi(x-k)\}_{k \in \mathbb{Z}} \text{ is a stable basis for } V_0
\end{aligned} \tag{4.7}$$

The interpretation of equation 4.7 is similar to a telescope: a fine scale is resolved via addition of more details. The fourth and fifth criteria states that one should look "with the same eyes" in all directions and at all scales. Finally the last criteria arise as a result of working in an infinite dimensional vector space [21].

4.3 Discrete Wavelet Domain

The Discrete Wavelet Transform (DWT) is a local filtering operation, decomposing the signal frequency content according to different scales [23], [24]. This transform is similar to Subband Coding in signal analysis but with specific constraints imposed on the filters coefficients. A brief summary is given using linear algebra for a 1D signal. A DWT of a 1D signal $\vec{x} = (x_1, \ldots, x_N)$ can be represented by a block circulant $N \times N$ matrix, W. The wavelet coefficient is simply $\vec{w} = W\vec{x}$. Inverse transformations (IDWT) are specified by $\tilde{W}$ where $\tilde{W}W = I$ and $\tilde{W} = W^T$ if the transform is orthogonal. The fundamental block F is a 2xL matrix where one row operates as a low pass filter and the other a high pass filter. The elements of F are chosen using quadrature mirror filter conditions and depend on the wavelet basis. Multi-level DWT can be computed using the pyramid algorithm [21].

Extension into 2D images can be interpolated from the result. The decomposition (or reconstruction) algorithm can be easily applied to two-dimensional (2-D) images by using the tensor product bases, transforming in row and column directions separately. Consequently, an image is decomposed into four subimages with a quarter area; one "approximated image," composed of the low-frequency parts in both row and column directions, and remaining three "detail images" containing high-frequency components. This is shown in figure 4.2

Compared to the Gabor and short-time Fourier transforms which use only a single window for all frequencies, wavelet transforms provide tradeoffs between time and space for different frequencies. At high frequencies, the wavelet transform is sharper in time while at low frequencies, the wavelet transform is sharper in frequency.

In general, restoring any image in this domain involves transforming the image

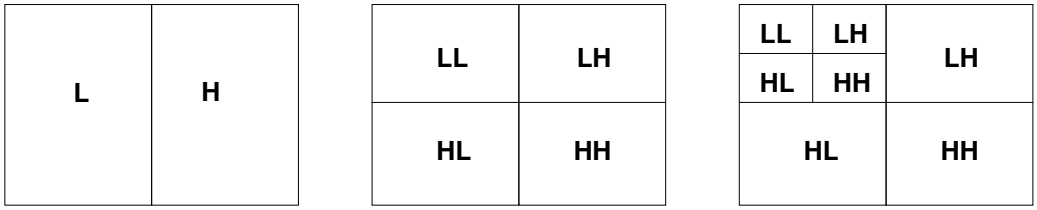

(a) Apply 1D wavelet tr form to rows

(b) Apply 1D wavelet tr form to columns

(c) Apply both row and column transform to $\tilde{h}$ in both directions

Figure 4.2: Two dimensional wavelet transform

into its wavelet representation and discarding some of the coefficients at each scale. After the inverse wavelet transform, the denoised image is presented [25]. Wavelet coefficient shrinkage creates a sparse data matrix, removing the noisy wavelet coefficients while preserving the large coefficients. The key to this process is the manipulation of the wavelet coefficients. Two popular thresholding schemes are hard and soft thresholding. Various strategies are employed (maximum SNR, regularization) to determine the threshold character which balances speckle suppression with detail signal preservation [26]. The homomorphic domain may also be used in the process to decouple the multiplicative nature of speckle noise in these multiscale algorithms. In the geoprocessing counterpart of this problem, statistical Markov Random Fields have also been applied to optimize the estimation of wavelet coefficients [8]. Complex wavelets have also been applied to mitigate speckle noise in the SAR counterpart of this problem due to it's overcomplete and symmetrical properties [27], [28]. The following sections discuss the complex wavelet transform and the dual tree complex wavelet transform.

4.4 Symmetric Complex Wavelets

By considering the complex wavelet domain, it is possible to take advantage of the symmetry in complex wavelets to determine the appropriate wavelet shrinkage using the phase. Complex Symmetric Daubechies (SD) wavelets are obtained by solving the complex multiresolution analysis formula as specified by equation 4.8.

$$\begin{aligned} \varphi(x) &= 2\sum_k a_k \varphi(2x-k) \\ \psi(x) &= 2\sum_k b_k \psi(2x-k) \end{aligned} \tag{4.8}$$

with

$$\begin{aligned} a_k &= a_{2N+1-k} \\ b_k &= (-1)^k a^*_{2N+1-k} \end{aligned}$$

for

$$\begin{aligned} N &= 0, 2, 4, 6, \ldots \\ k &= 0, \ldots, 2N+1 \end{aligned}$$

Complex SD wavelets have better interpolation capability then their real counter parts due to identical vanishing of the second centered moment of the real part of the scaling function [29].

In addition to orthogonality and compact support, the Complex Symmetric Daubechies wavelets are also symmetric. This symmetry, possible when complex valued scaling functions are considered, implies that the real and imaginary part of the wavelet functions are of odd parity with respect to the center of the support while the real and imaginary part of the scaling function is of even parity. A

consequence of this symmetric property limits the set to even values of N.

Symmetry is desired for image processing applications as it allows for symmetric data extensions at the image boundaries. Symmetric extensions prevent discontinuities introduced by a periodic wrapping of the data. Apart from slight increases in computational workload, the complex transform does not have any drawbacks. Like Fourier analysis, Symmetric Daubechies wavelets introduce redundancy in the transform of a real signal but this can be used in an advantageous way for design. SD wavelets are selected in this paper mainly because of their symmetry properties.

Complex Daubechies Wavelets also possess a hidden Laplacian kernel that allows them to be used as a local multiresolution sharpening operator. The SD wavelets has simultaneous a smoothing kernel and its Laplacian in the complex scaling function, providing additional benefits to improving image resolution [29]. Figure 4.3 shows an example of the complex Daubechies mother wavelet and scaling function for $N = 6$.

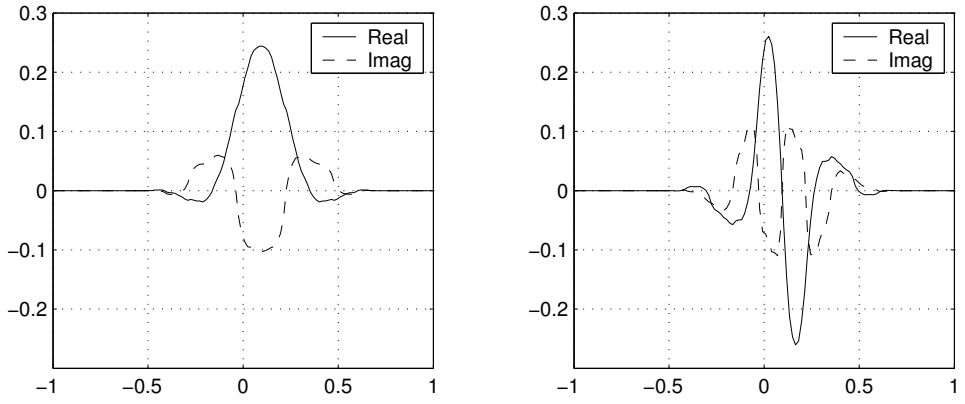

Figure 4.3: A complex scaling function (left) and wavelet (right) for N=6

4.5 Dual Tree Symmetric Complex Wavelets

One desirable property not addressed by the discrete and complex wavelet transform discussed thus far is that they represent shift variant systems. This implies that the results of the denoising operation will depend on the starting point of the signal and lead to artifacts referred to as the Gibbs phenomena. A number of solutions have been proposed by researchers to produce shift invariant wavelet transforms. These methods attempt to reduce the aliasing introduced by a combination of relaxing the critical subsampling criteria and reducing the transition bandwidth of the mother filters. One method, avoiding subsampling altogether is referred to as the algorithme a trous [20]; however, the computational load is dramatically increased and is only shift invariant under circular convolution (periodic boundary extension). Another includes the cycle-spinning concept proposed by Coifman and Donoho. [30] Other strategies include the Laplacian pyramid [20] and the continuous wavelet transform [21]. In this investigation, we study the dual tree complex wavelet transform introduced by Kingsbury [31] which can provide shift invariance and added directional selectivity with a modest increase in signal redundancy and computation load.

The complex dual-tree discrete wavelet transforms introduced in [31] is implemented using two critically-sampled DWTs in parallel as shown in figure 4.4. The upper and lower DWT subband signals can be interpreted as the real and imaginary component of a complex wavelet transform respectively. Designing the filters as described by [32] generates an approximate Hilbert transform with nearly shift invariant properties. In addition, the DT CWT create oriented wavelets, providing good directional selectivity. The directional selectivity comes about without explicitly rotating a filter as in a Gabor filter bank.

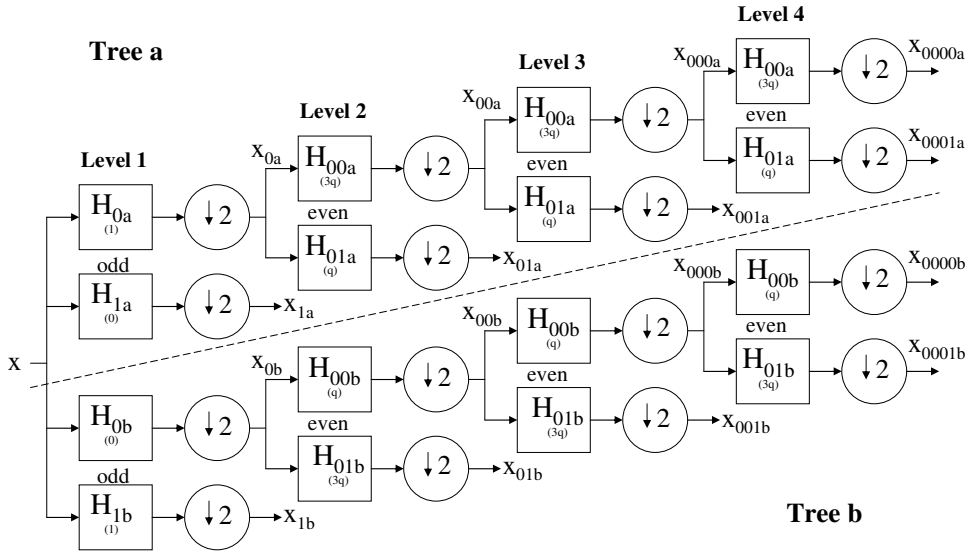

Figure 4.4: 1D Dual tree complex wavelet transform of Kingsbury [33]

The 1D dual-tree complex wavelet decomposes a signal $x(t)$ in terms of a complex shifted and dilated mother wavelet according to equation 4.9 where j represents the decomposition level and l the translation.

$$\begin{aligned} x(t) &= \sum_{l\in\mathbb{Z}} u_{j_0,l}\phi_{j_0,l}(t) + \sum_{j\le j_0}\sum_{l\in\mathbb{Z}} c_{j,l}\psi_{j,l}(t) \\ \phi_{j_0,l} &= \phi^r_{j_0,l} + i\phi^i_{j_0,l} \\ \psi_{j,l} &= \psi^r_{j,l} + i\psi^i_{j,l} \end{aligned} \tag{4.9}$$

$\phi_{j_0,l}$ and $\psi_{j,l}$ represent the scaling and wavelet functions respectively. The $u_{j_0,l}$, and $c_{j,l}$ represents the coarse and detail coefficients respectively. Note that $\{\phi^r_{j_0,l}, \phi^i_{j_0,l}, \psi^r_{j,l}, \psi^i_{j,l}\}$ are real numbers. Due to technicalities, the filters in the first stage of the DT CWT are different from the remaining stages [31]. The proposed implementation uses the farras wavelet, $\{H_{0a}, H_{1a}\}$ and $\{H_{0b}, H_{1b}\}$, for the first decomposition stage as shown in figure 4.4 [9]. The real, imaginary, and magnitude components of

the wavelet used in subsequent stages is shown in figure 4.3. Note that the imaginary basis functions share the same locale, but are 90° out of phase, implying that real and imaginary basis functions will be odd and even functions, respectively, or vice versa. The real and imaginary parts of the DT CWT are computed using separate filter bank structures with wavelet filters $\{H_{00a},\ H_{01a}\}$ and $\{H_{00b},\ H_{01b}\}$ as shown in figure 4.4.

The 2D complex discrete wavelet transform produces a pyramid of complex sub images as defined in equation 4.10. Assume $x(\mathbf{p})$ is an image with $\mathbf{p} = (p_1, p_2)$.

$$x(\mathbf{p}) \quad = \quad \sum_{l\in\mathbb{Z}^2} u_{j_0,l}\phi_{j_0,l}(\mathbf{p}) + \sum_{b\in\beta}\sum_{j\leq j_0}\sum_{l\in\mathbb{Z}^2} c^b_{j,l}\psi^b_{j,l}(\mathbf{p}) \tag{4.10}$$

The notation definitions are identical to the 1D case. In addition, there are six evenly spaced orientation sub images at each level labelled $\beta = \{15°, 45°, 75°, -15°, -45°, -75°\}$. Note that subsequent analysis has shown that these orientations may vary depending on scale [34]. Regardless of exact orientation, the six wavelets in the 2D complex wavelet transform provides a greater directional selectivity than the traditional DWT. For example, an edge in a image at a 15° angle causes the CD CWT coefficients in the $\psi^{15°}(\mathbf{p})$ to be large. Edges oriented at −15° will produce large coefficients in $\psi^{-15°}(\mathbf{p})$. However, in the DWT decomposition, both of these edges would cause the real coefficient in the 0° (horizontal) subband to be large.

The six distinct wavelet orientations are shown in figure 4.5. The first and second row represents the real and imaginary components of the wavelet and the third row reveals the magnitude of the complex wavelets. Notice that the complex wavelets are not oscillatory and have bell shaped envelopes. The coefficients are based on a region in the original image corresponding to the spatial extent of the

filter $\psi^{(n)}$. Based on 1D complex ϕ and ψ, the relationship between 1D and 2D DT CWT is revealed by equation 4.11. Note that x^* is the conjugate of x.

$$\begin{aligned}
\psi^{15^\circ}(\mathbf{p}) &= \phi(\mathbf{p}_1)\psi(\mathbf{p}_2) \\
\psi^{45^\circ}(\mathbf{p}) &= \psi(\mathbf{p}_1)\psi(\mathbf{p}_2) \\
\psi^{75^\circ}(\mathbf{p}) &= \psi(\mathbf{p}_1)\phi(\mathbf{p}_2) \\
\psi^{-15^\circ}(\mathbf{p}) &= \phi(\mathbf{p}_1)\psi^*(\mathbf{p}_2) \\
\psi^{-45^\circ}(\mathbf{p}) &= \psi(\mathbf{p}_1)\psi^*(\mathbf{p}_2) \\
\psi^{-75^\circ}(\mathbf{p}) &= \psi(\mathbf{p}_1)\phi^*(\mathbf{p}_2)
\end{aligned} \tag{4.11}$$

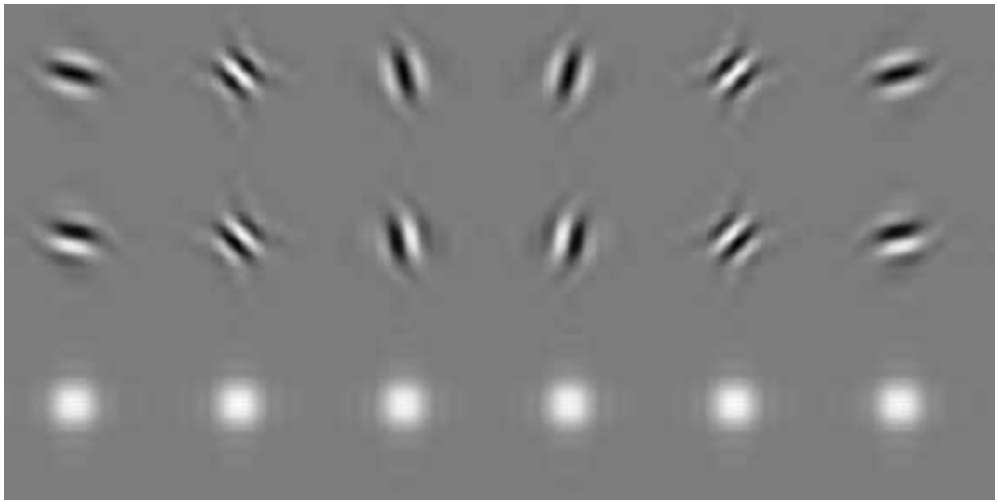

Figure 4.5: Real and imaginary impulse response of wavelet filters of [31]

The penalty paid for DT CWT is a 2:1 increase in redundancy per signal dimension. The redundancy is the presence of a second tree shown in figure 4.4 below the dotted lines for 1D CDWT. [31]

4.6 A Statistical Model of Complex Wavelet Coefficients

Let $C(\mathbf{p})$ be considered as the contribution of speckle noise with Rayleigh distributed speckle to the image texture, $\hat{A}X(\mathbf{p})$ where $\hat{A}$ represents the average amplitude of the target and $X(\mathbf{p})$ the normalized image texture. For analysis of first order statistics, we assume the texture to be unity to analyze the noise contribution. Under these assumptions, we can reestablish equation $Y = CX$ as:

$$Y(\mathbf{p}) = \hat{A}C(\mathbf{p}) \tag{4.12}$$

Therefore, the wavelet coefficients are

$$c_{j,l} = \hat{A}\int C(\mathbf{p})\psi_{j,l}(\mathbf{p})d\mathbf{p} \tag{4.13}$$

Similar to the wavelet coefficients in the real domain analyzed by Simard [35], the mean amplitude of the fading signal is directly proportional to the wavelet coefficients. At scale j, the integral from equation 4.13 will also be a nonvanishing function of l since $C(\mathbf{p})$ has finite energy and $\int_{-\infty}^{+\infty}\psi_{j,l} = 0$, establishing the dependence of the $c_{j,l}$ on $\hat{A}$.

In the log normal case, the noise becomes additive such that

$$\hat{Y}(\mathbf{p}) = \hat{A}\hat{T}(\mathbf{p}) + \hat{C}(\mathbf{p}) \tag{4.14}$$

Therefore, the wavelet coefficients are

$$c_{j,l} = \hat{A}\int T(\mathbf{p})\psi_{j,l}(\mathbf{p})d\mathbf{p} + \int C(\mathbf{p})\psi_{j,l}(\mathbf{p})d\mathbf{p} \tag{4.15}$$

The noise term is given by the second integral in equation 4.15. It contributes an equal amount to the wavelet coefficient for different homogeneous areas regardless of the average amplitude.

In an attempt to gain some insight into the nature of correlated speckle noise, we consider the power spectrum density of a linear space-invariant system given in equation 4.16.

$$P_w(\mathbf{w}) \quad = \quad P_s(\mathbf{w})|\Psi(\mathbf{w})|^2 d\mathbf{w} \tag{4.16}$$

where $P_s(\mathbf{w})$ is the speckle noise power spectrum equal to the Fourier transform of its autocorrelation. [35] This analysis is valid as wavelets can be considered well localized in the frequency domain. Furthermore, by the convolution theorem, the wavelet coefficients is equal to the product of the Fourier transform of the signal and the Fourier transform of the wavelet filter response. Since the speckle is correlated, the power density spectrum is not flat. Therefore, coefficients will show dependence on the correlation.

Often, a speckled image is denoised by averaging L uncorrelated amplitude samples from linear detection to form a multilook image. Under these conditions, the pdf can be obtained numerically by successive convolutions of L identical Rayleigh distributions. [8] As established in other papers [36], as the number of looks increases, the speckle random variable approaches a Gaussian distribution. In the follow section we investigate the wavelet coefficients at various levels to draw parallel between the real wavelets and complex wavelet decompositions.

4.7 Empirical Comparisons of Complex Wavelet Coefficients

In this section, a simple statistical model of an multilook ultrasound image with correlated speckle will be used to evaluate the contribution of speckle on the complex wavelet coefficients. Figure 4.6, showing both the intensity domain and homomorphic domain images, is used in the following analysis. Figure 4.7 displays the PDF of the wavelet coefficients for the SD complex wavelet transform as a function of phase and amplitude. The complex coefficients at each level is divided into 160(40x40) linearly spaced 2D bins based on its magnitude and phase. By decoupling the phase and amplitude for each coefficient, we can attempt to model the amplitude and phase using known distributions independently. Log transformed data is also analyzed in figure 4.8, which shows the 2D PDF, the marginal phase PDF, and amplitude PDF of the wavelet coefficient following a logarithmic transformation of the original image. By observing figures 4.7 and 4.8 and by theoretical analysis above, the magnitude of the coefficients seem to follow a Rayleigh distribution while the phase appears bimodal which we will attempt to model using a mixed Gaussian distribution.

To quantify the statistical variation of the complex wavelet coefficients in phase and amplitude, we apply the maximum likelihood estimator. The maximum likelihood parameters are found by maximizing equation 4.17

$$\hat{\theta}_{ML} \quad = \quad arg\left\{\max_{\theta \epsilon \Theta} \; p(\mathbf{x}|\theta)\right\} \tag{4.17}$$

where $p(\mathbf{x}|\theta)$ denotes the probability density function of data-vector $\mathbf{x}$ parameterized by the parameter vector θ. The Cramer Rao Lower Bound for the unbiased

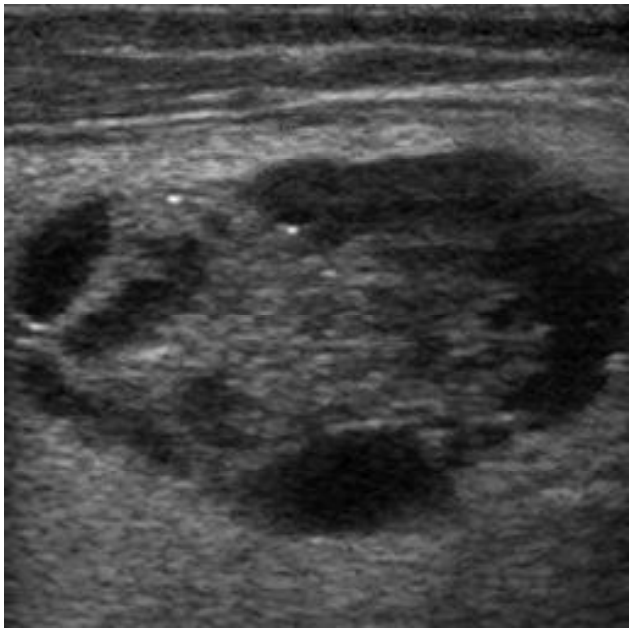

(a) Amplitude Image

(b) Logarithmic Transformed

Figure 4.6: Representative Ultrasound Image

estimator is calculated to characterize the error variance in the amplitude Rayleigh modelling case. The RMS error is also calculated for the amplitude modelling to provide an indication of the goodness of fit. Equation 4.18 shows the details of the RMS calculation.

$$RMS = \sqrt{\frac{1}{n}\frac{(y_p - y_o)(y_p - y_o)'}{(x_2 - x_1)^2}}; \tag{4.18}$$

where n represents the number of samples, y_p represents the predicted value, y_o represents the observed value, and $x_2 - x_1$ represents the change in the x direction from sample to sample. The Rayleigh model is fitted to equation 4.19

$$p(x, s) = \frac{x}{s} \exp\left(-\frac{x^2}{2s}\right) \tag{4.19}$$

The mix Gaussian model used to approximate the phase distribution is characterized by the number of iterations required to reach a minimum. A percentage indicating the relative weighing of the Gaussian curve is included in the numerical analysis. The mixed Gaussian fit is accomplished application of the EM algorithm. [37] Each EM iteration consists of an E-step and and M-step. The E step is to evaluate the probability distribution given the model parameters, and the M step maximizes the current parameters. Although the two steps will converge, only a local maximum can be guaranteed by the EM algorithm. The resulting numerical analysis of the image in the intensity domain and homomorphic domain for the SD complex wavelet are shown in table 4.1, 4.2 and table 4.3, 4.4 respectively.

Data from the intensity domain analysis (tables 4.1 and 4.2) shows that the probability distributions used to model the wavelet coefficients have potential. In the phase modelling, we attempt to model the data as two Gaussian distributions. We see that only a few iterations are required for the EM algorithm to converge although the Gaussian fit is not perfect. Figure 4.7 shows that the approximation

Table 4.1: ML Mixed Gaussian Parameters and Estimation Error in phase for SD Complex Wavelets Analysis using Ultrasonic Images

SD CWT	Intensity Domain						
	mean, μ_1	std dev, σ_1	percentage	mean, μ_2	std dev, σ_2	percentage	iteration
level 1 HH	-2.3860	0.4006	39.43	0.8433	1.0516	60.57	93
level 1 HL	-2.7433	0.2286	33.89	0.5224	1.2300	66.11	89
level 1 LH	-2.7161	0.2190	39.22	0.5580	1.0904	60.78	76

Table 4.2: ML Rayleigh Amplitude Estimates and RMS Error for SD Complex Wavelet Analysis using Ultrasonic Images

SD CWT	Intensity Domain		
	parameter, s	CR Bound	RMS error
level 1 HH	0.4857	5.7587e-005	4.0815
level 1 HL	4.9559	0.0060	0.1857
level 1 LH	31.0316	0.2351	0.0404

for the phase is fairly accurate although applying a mixture of 3 Gaussian distribution may better fit the data. However, this comes at the expense of computational load. The amplitude Rayleigh data also shows promise, as RMS error values are not very large.

Data from the density domain analysis (tables 4.3 and 4.4) show similar trends to the intensity domain analysis. However, the amplitude RMS error values have increased dramatically. This is due to the decrease in the $x_2 - x_1$ values as evident in Figure 4.8. The small amplitude distribution causes an increase in the RMS error although graphical results seems to show a descent fit. Further investigation into the log transformed amplitude distribution is required before any further conclusions can be drawn concerning the validity of Rayleigh models.

Table 4.3: ML Mixed Gaussian Parameters and Estimation Error in phase for SD Complex Wavelets using Log Transformed Images

SD CWT	Density (Homomorphic) Domain						
	mean, μ_1	std dev, σ_1	percentage	mean, μ_2	std dev, σ_2	percentage	iteration
level 1 HH	-2.3896	0.4055	40.57	0.8295	1.0152	59.43	80
level 1 HL	-2.7465	0.2291	34.21	0.5202	1.2202	65.79	82
level 1 LH	-2.7218	0.2130	38.82	0.5468	1.1144	61.18	72

Table 4.4: ML Rayleigh Estimates and RMS Error in Amplitude for SD Complex Wavelet Analysis using Log Transformed Images

SD CWT	Density (Homomorphic) Domain		
	parameter, s	CR Bound	RMS error
level 1 HH	1.7870e-005	7.7962e-014	8.4866e+004
level 1 HL	1.5197e-004	5.6382e-012	7.2054e+003
level 1 LH	8.5881e-004	1.8007e-010	1.5637e+003

The effects of DT complex wavelet decomposition on wavelet coefficients were also analyzed. Figure 4.9 displays the PDF and the Gaussian estimation of the wavelet coefficients for the DT complex wavelet transform. The complex coefficients at each level is divided into 160(40x40) linearly spaced 2D bins based on its magnitude and phase. Figure 4.11 shows the PDF of the same image following a logarithmic transformation. In both the intensity and density domain cases, the distribution of wavelet coefficients appears similar. To quantify the statistical variation of the dual tree complex wavelet coefficients phase and amplitude from the mixed Gaussian and Rayleigh distribution, we apply the maximum likelihood estimator as before. ML estimators are unbiased minimum variance estimators used to test hypotheses about models and parameters. Table 4.5 and table 4.6 shows the

numerical analysis for the intensity domain transformations. The statistical results for the log transformed image is shown in table 4.7 and 4.8.

Table 4.5: Phase ML Gaussian Parameter Estimates and RMS Error in DT Complex Wavelet Analysis for Intensity Domain Images

DT CWT	Intensity Domain						
	mean, μ_1	std dev, σ_1	percentage	mean, μ_2	std dev, σ_2	percentage	iteration
$\psi^{15^\circ}(\mathbf{p})$	-1.2707	1.0826	58.48	1.8050	0.8267	41.52	1968
$\psi^{45^\circ}(\mathbf{p})$	-1.9341	0.7221	34.45	1.0136	1.2132	65.55	1874
$\psi^{75^\circ}(\mathbf{p})$	-1.6372	0.9898	50.22	1.3517	1.0467	49.78	10
$\psi^{-15^\circ}(\mathbf{p})$	-1.3389	1.0665	54.36	1.6747	0.8745	45.64	1947
$\psi^{-45^\circ}(\mathbf{p})$	-1.7625	0.8055	40.26	1.1987	1.1341	59.74	1143
$\psi^{-75^\circ}(\mathbf{p})$	-2.2925	0.5322	24.32	0.7143	1.4436	75.68	864

Table 4.6: ML Mixed Gaussian Parameter Estimates and RMS Error in Amplitude DT Complex Wavelet Analysis for Intensity Domain Images

DT CWT	Intensity Domain		
	parameter, s	CR Bound	RMS error
$\psi^{15^\circ}(\mathbf{p})$	32.6786	1.0429	0.0289
$\psi^{45^\circ}(\mathbf{p})$	203.7547	40.5430	0.0062
$\psi^{75^\circ}(\mathbf{p})$	14.2679	0.1988	0.1019
$\psi^{-15^\circ}(\mathbf{p})$	30.7566	0.9238	0.0304
$\psi^{-45^\circ}(\mathbf{p})$	200.6151	39.3032	0.0061
$\psi^{-75^\circ}(\mathbf{p})$	12.7881	0.1597	0.0712

The results from the DT CWT intensity domain analysis (tables 4.5 and 4.6 and figure 4.9) were not as encouraging as that of the SD CWT results. The phase analysis showed little bimodal characteristics. As a result, the mixed Gaussian model required many EM iterations to converge. Although it does not seem possible to apply the same phase model as the SD CWT wavelets, the Rayleigh modelling

Table 4.7: Phase ML Mixed Gaussian Parameter Estimates and RMS Error in DT Complex Wavelet Analysis for Log Transformed Images

DT CWT	Density (Homomorphic) Domain						
	mean, μ_1	std dev, σ_1	percentage	mean, μ_2	std dev, σ_2	percentage	iteration
$\psi^{15^\circ}(\mathbf{p})$	-1.3127	1.0663	0.5828	1.7810	0.8260	0.4172	1226
$\psi^{45^\circ}(\mathbf{p})$	-1.9811	0.6798	0.3297	0.9984	1.2289	0.6703	884
$\psi^{75^\circ}(\mathbf{p})$	-2.0781	0.6855	0.3325	0.8829	1.3228	0.6675	1269
$\psi^{-15^\circ}(\mathbf{p})$	-1.6001	0.9060	0.4505	1.4164	1.0349	0.5495	1484
$\psi^{-45^\circ}(\mathbf{p})$	-1.8036	0.7986	0.4014	1.1813	1.1088	0.5986	787
$\psi^{-75^\circ}(\mathbf{p})$	-2.2711	0.5978	0.2600	0.7190	1.4001	0.7400	761

Table 4.8: ML Mixed Gaussian Parameter Estimates and RMS Error in Amplitude Dual Tree Complex Wavelet Analysis for Log Transformed Images

DT CWT	Density (Homomorphic) Domain		
	parameter, s	CR Bound	RMS error
$\psi^{15^\circ}(\mathbf{p})$	9.2062e-004	8.2767e-010	939.8648
$\psi^{45^\circ}(\mathbf{p})$	0.0055	2.9188e-008	283.9761
$\psi^{75^\circ}(\mathbf{p})$	4.4308e-004	1.9172e-010	4.4577e+003
$\psi^{-15^\circ}(\mathbf{p})$	8.6488e-004	7.3049e-010	1.0764e+003
$\psi^{-45^\circ}(\mathbf{p})$	0.0054	2.7960e-008	324.4319
$\psi^{-75^\circ}(\mathbf{p})$	3.9836e-004	1.5497e-010	3.2468e+003

of the DT CWT coefficients seemed adequate as they generated small RMS error values.

In analyzing the density domain results, we find from tables 4.7 and 4.8 and figure 4.11 that both the phase and amplitude modelling via the mixed Gaussian and Rayleigh distributions do not accurately reflect the underlying distributions. More analysis is required in order to model the DT complex wavelet coefficients.

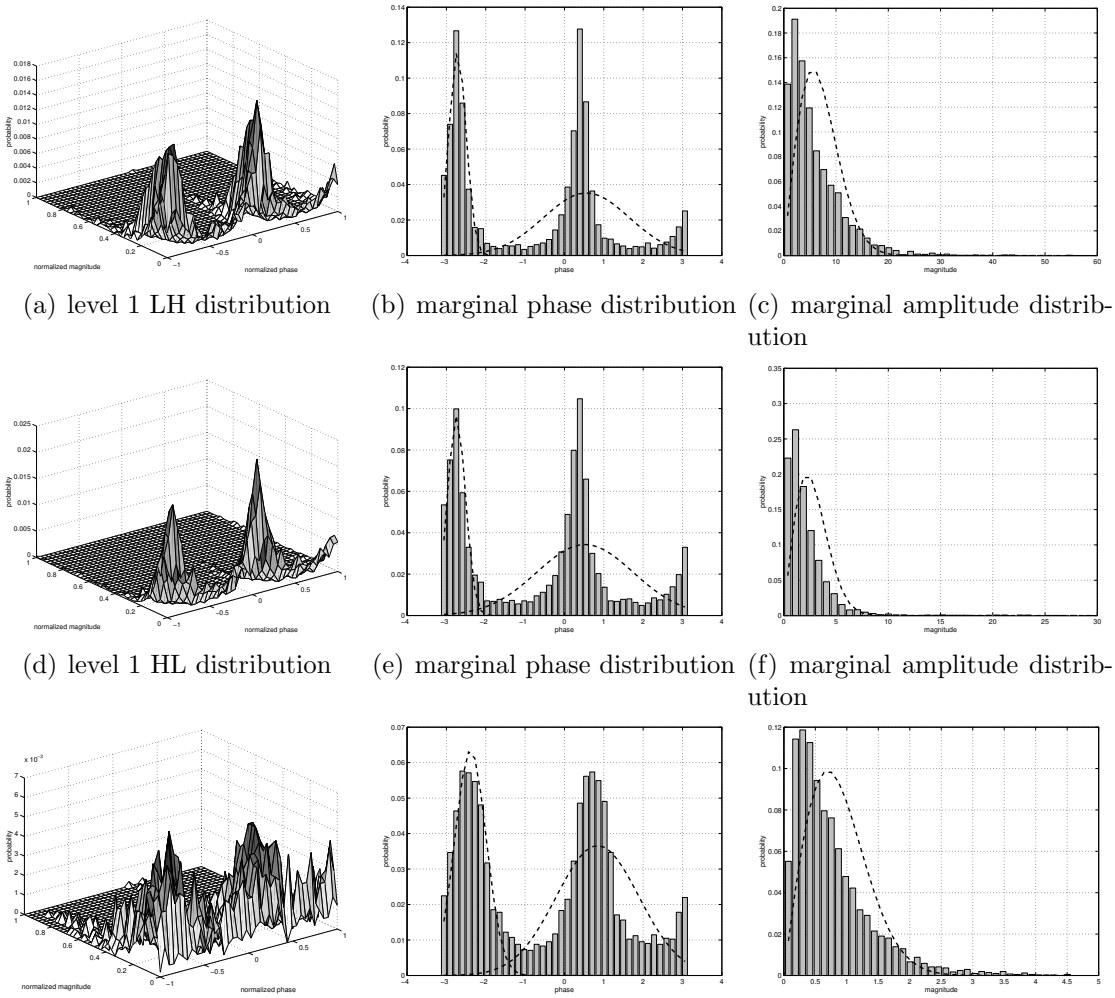

(a) level 1 LH distribution (b) marginal phase distribution (c) marginal amplitude distribution

(d) level 1 HL distribution (e) marginal phase distribution (f) marginal amplitude distribution

(g) level 1 HH distribution (h) marginal phase distribution (i) marginal amplitude distribution

Figure 4.7: 2D and Marginal PDF of SD CWT Wavelet Coefficients (bar graph) and the ML Gaussian Probability Approximation (dotted) for the representative ultrasound image

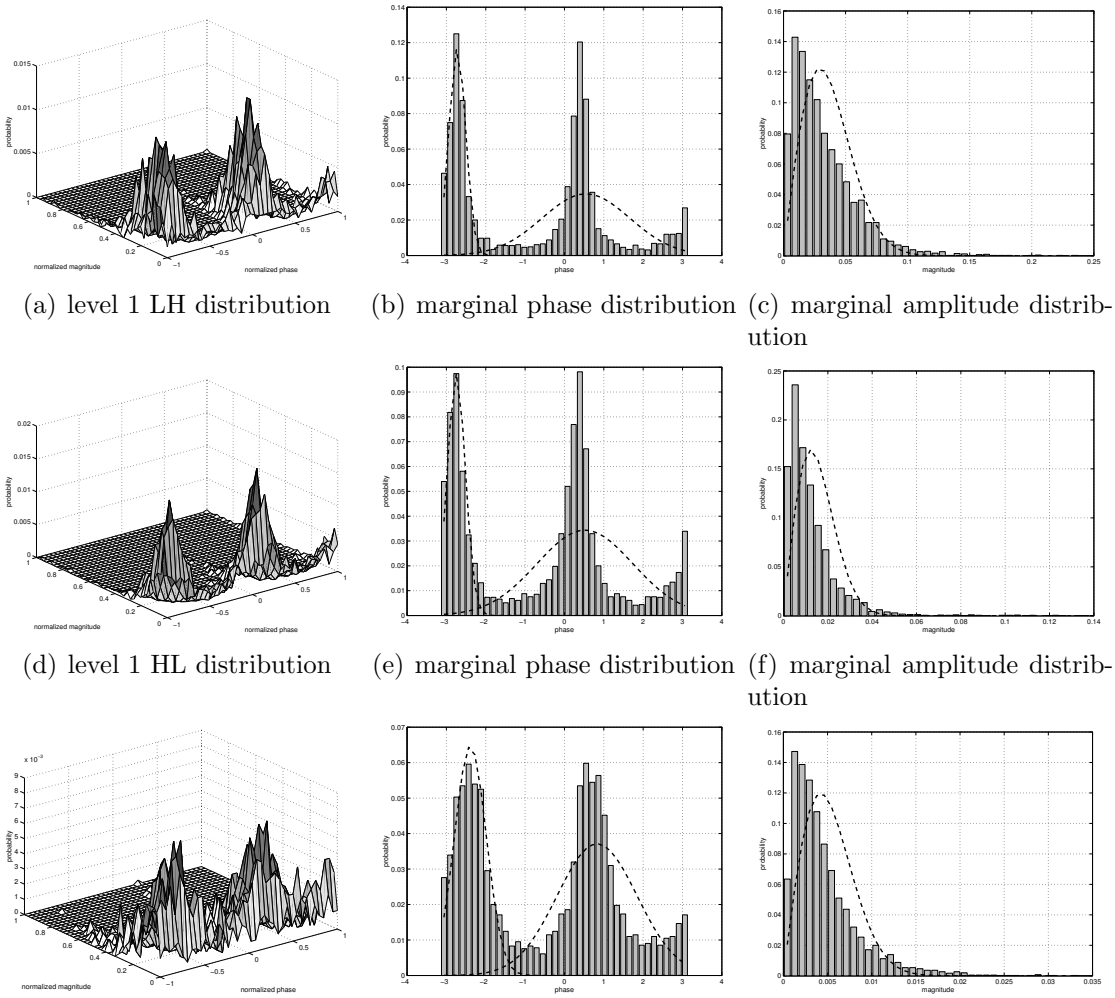

(a) level 1 LH distribution (b) marginal phase distribution (c) marginal amplitude distribution

(d) level 1 HL distribution (e) marginal phase distribution (f) marginal amplitude distribution

(g) level 1 HH distribution (h) marginal phase distribution (i) marginal amplitude distribution

Figure 4.8: 2D and Marginal PDF of SD CWT Wavelet Coefficients (bar graph) and the ML Gaussian Probability Approximation (dotted) for the homomorphic processed ultrasound image

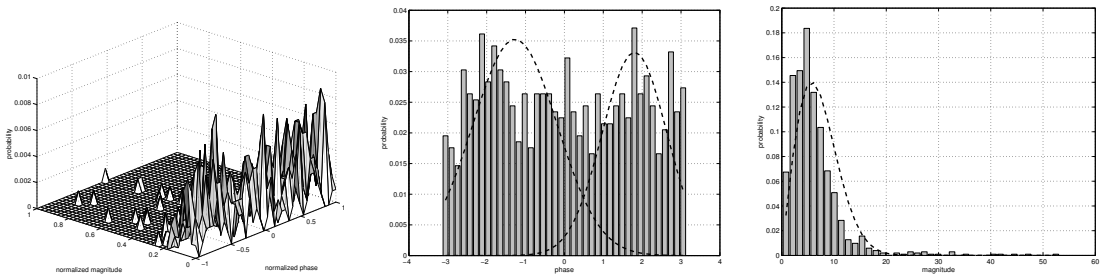

(a) level 2 $\psi^{15^\circ}(\mathbf{p})$ distribution (b) marginal phase distribution (c) marginal amplitude distribution

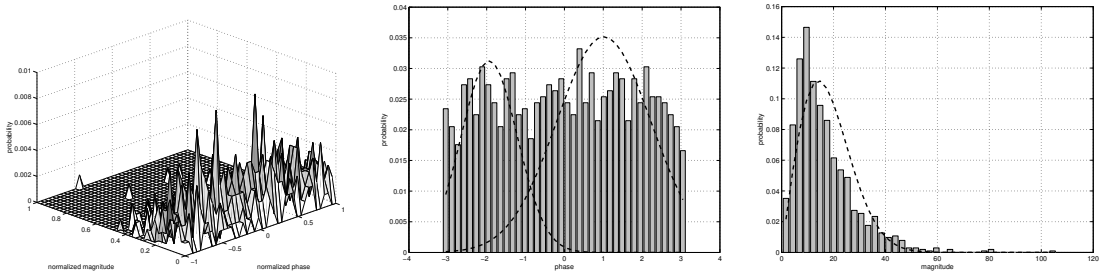

(d) level 2 $\psi^{45^\circ}(\mathbf{p})$ distribution (e) marginal phase distribution (f) marginal amplitude distribution

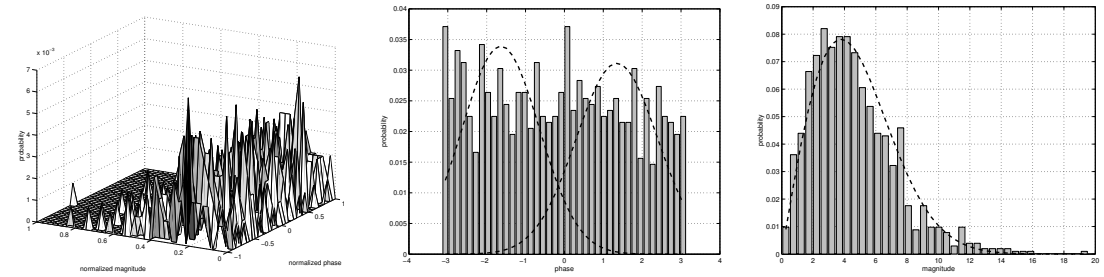

(g) level 2 $\psi^{75^\circ}(\mathbf{p})$ distribution (h) marginal phase distribution (i) marginal amplitude distribution

Figure 4.9: 2D and Marginal PDF of DT CWT Wavelet Coefficients (bar graph) and the ML Gaussian Probability Approximation (dotted) for the Representative Ultrasound Image

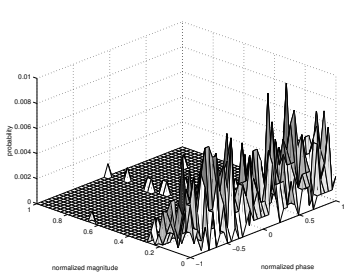

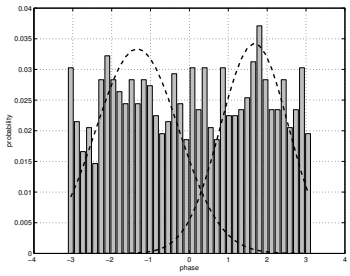

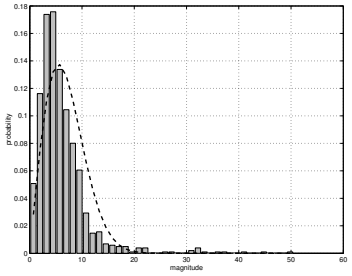

(j) level 2 $\psi^{-15^\circ}(\mathbf{p})$ distribution (k) marginal phase distribution (l) marginal amplitude distribution

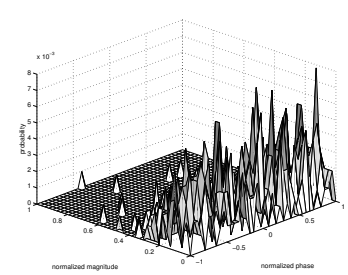

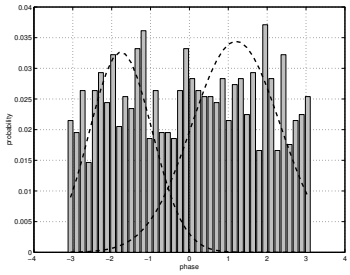

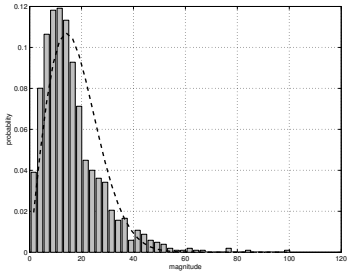

(m) level 2 $\psi^{-45^\circ}(\mathbf{p})$ distribution (n) marginal phase distribution (o) marginal amplitude distribution

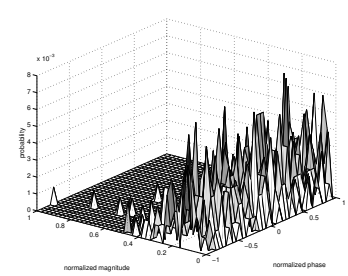

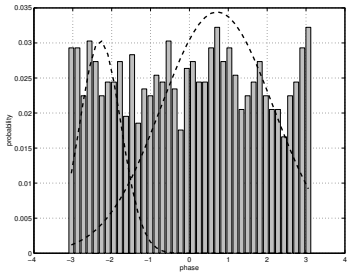

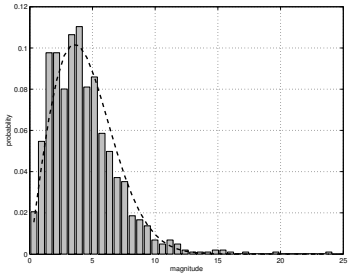

(p) level 2 $\psi^{-75^\circ}(\mathbf{p})$ distribution (q) marginal phase distribution (r) marginal amplitude distribution

Figure 4.10: 2D and Marginal PDF of DT CWT Wavelet Coefficients (bar graph) and the ML Gaussian Probability Approximation (dotted) for the Representative Ultrasound Image (cont)

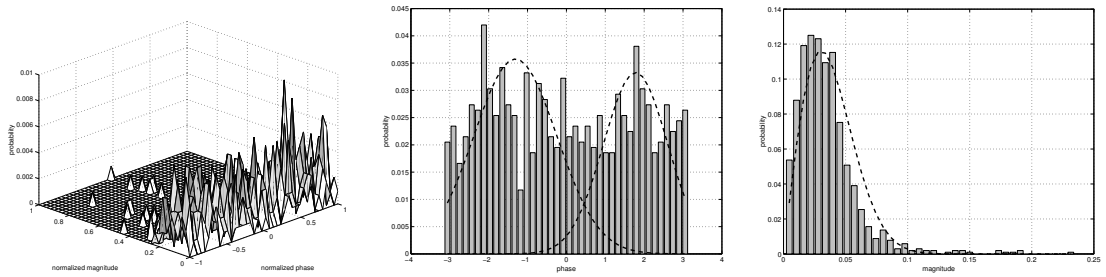

(a) level 2 $\psi^{15^\circ}(\mathbf{p})$ distribution (b) marginal phase distribution (c) marginal amplitude distribution

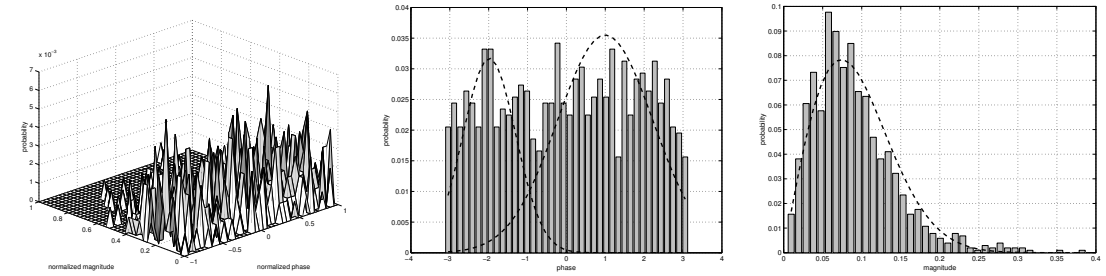

(d) level 2 $\psi^{45^\circ}(\mathbf{p})$ distribution (e) marginal phase distribution (f) marginal amplitude distribution

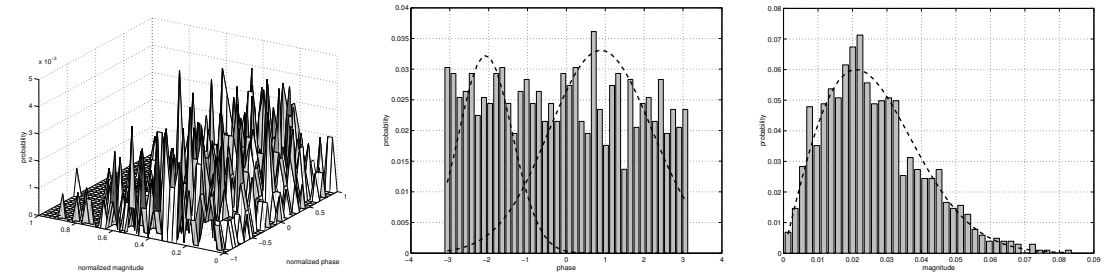

(g) level 2 $\psi^{75^\circ}(\mathbf{p})$ distribution (h) marginal phase distribution (i) marginal amplitude distribution

Figure 4.11: 2D and Marginal PDF of DT CWT Wavelet Coefficients (bar graph) and the ML Gaussian Probability Approximation (dotted) for the homomorphic processed ultrasound image

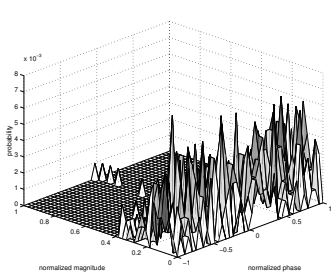

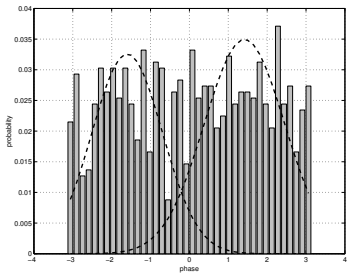

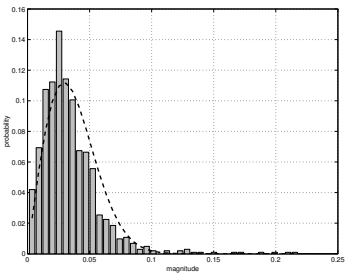

(j) level 2 $\psi^{-15^\circ}(\mathbf{p})$ distribution (k) marginal phase distribution (l) marginal amplitude distribution

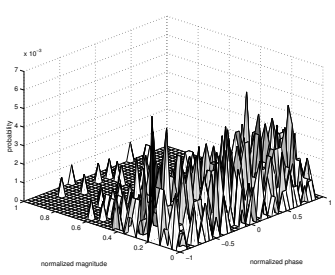

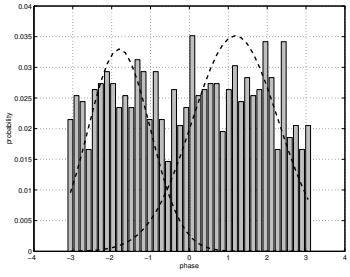

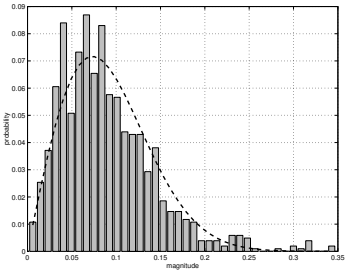

(m) level 2 $\psi^{-45^\circ}(\mathbf{p})$ distribution (n) marginal phase distribution (o) marginal amplitude distribution

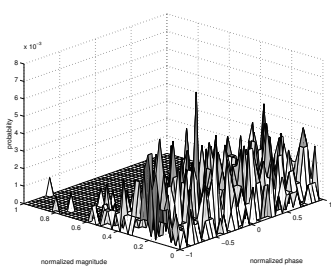

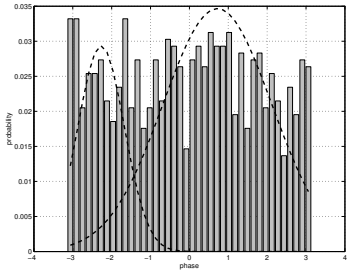

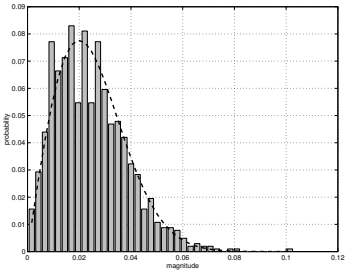

(p) level 2 $\psi^{-75^\circ}(\mathbf{p})$ distribution (q) marginal phase distribution (r) marginal amplitude distribution

Figure 4.12: 2D and Marginal PDF of DT CWT Wavelet Coefficients (bar graph) and the ML Gaussian Probability Approximation (dotted) for the homomorphic processed ultrasound image (cont)

4.8 Summary

This chapter investigated wavelet theory and various properties of the wavelet transform. It also discussed the discrete wavelet domain and summarized developed by Lina [29] and Kingsbury [31] the theory which extended from the real to the complex domain in the discussion of symmetric complex wavelets and dual tree symmetric complex wavelets. Finally, Newly developed models for the complex wavelets coefficients of speckle noise is derived and discussed for both the complex symmetric wavelet and the dual tree complex wavelet transform. The next chapter uses the theory discussed here and introduces the proposed noise reduction algorithm referred to as an elliptically thresholded rotation.

Chapter 5

Elliptically Thresholding and Rotating (ETR) Algorithm

The speckle-corrupted image may be denoised via multi-resolution signal processing, by transforming the image into a wavelet domain, wherein the image's wavelet-coefficients are thresholded [38], [22], [39], [27]. These wavelet-coefficients generally have large magnitudes in image-regions containing many edges, but small magnitudes in image-regions with uniform spatial intensity. As high spatial-frequency information is embedded in the "detailed coefficients", noise would be more prominent in these "detailed coefficients" than in the "approximate coefficients", which correspond to low spatial frequencies. Zeroing those detailed coefficients below a certain magnitude-threshold (and perhaps reducing all other coefficients by the threshold value), An inverse-wavelet-transform would then produce a denoised image. Thresholding discards noise-dominated wavelet-coefficients but retains signal-dominated wavelet-coefficients, resulting in "wavelet coefficient shrinkage" [38]. Thresholding is predicated on these assumptions regarding the noise:

1. The noise energy is about equally spread over all wavelet-coefficients.

2. The noise variance is not excessively high at various wavelet-coefficients to forestall identification of wavelet-coefficients of significant image-signal energy.

Note that the decorrelating property of the wavelet transform will create a sparse signal so that most untouched coefficients are zero or close to zero. Signal and image denoising in transform domain consists of three general steps:

1. Transformation of input data by an orthogonal transform.

2. Modification of transform coefficients by a nonlinear algorithm.

3. Inverse transformation of the modified coefficients.

5.1 Noise Reduction by Thresholding Wavelet Coefficients

If an orthogonal transform which has high energy compaction and decorrelation properties is used, most of the energy of the original signal will be compacted into a few high magnitude coefficients. If the input data is corrupted by additive white noise, components which correspond to noise will be distributed among low magnitude high frequency components. Hence, a thresholding algorithm in an orthogonal transform domain will remove most of the noise components. The transfer from signal domain into the transform domain is especially promising if it is applied locally rather than globally. Local transform domain denoising apply the three steps listed above in a moving window for obtaining an estimate of the central pixel of

the window. Recently, nonlinear filtering in wavelet transform domain has been introduced in terms of wavelet denoising and found efficient applications in restoration of different types of images ranging from medical imaging to synthetic aperture radar.

If complex-value wavelets (e.g., the symmetric-Daubechies wavelets) are used, thresholding may exploit any complex-phase information embedded in the complex-value wavelet-coefficients [39], [27], rather than being limited to any real-value wavelet-coefficients' magnitudes. With a complex-value wavelet transformation, thresholding could be based only on the complex-value wavelet-coefficients' real-value part [27], but that would waste any information in the complex-value wavelet-coefficients' imaginary-value part. The real-value and the imaginary-valued parts can both be utilized with a two-dimensional threshold defined on the complex-plane, e.g., an elliptical-ring [39] [1]. Because the wavelet-coefficients' real-value and imaginary-value parts are approximately bi-normal with non-zero means on the complex-plane [39], the two-dimensional threshold becomes a elliptical ring, with the elliptical axes aligned with the binormal distribution's orientation on the complex-plane [39].

When an image is corrupted by multiplicative noise, the corrupted image's homomorphic-domain's wavelet-coefficients' elliptical axes rotate from those of the original image [39]. Hence, this work proposes a counter-rotation of the corrupted-image's elliptical axes as a denoising strategy.

[1] Speckle-noise intensity on field-collected synthetic-aperture radar (SAR) images are found to be approximately Gamma-distributed [40], or approximately log-normal distributed [39]. Nonetheless, an image's actual speckle-noise intensity distribution does not much affect the performance of the aforementioned symmetric-Daubechies-wavelet-thresholding denoising algorithms [39]. Moreover, with a large number of scatterers per pixel, the imaging system develops the full speckle characteristic of spatially uncorrelated pixel brightness.

5.2 The Homomorphic Domain

Homomorphic filtering is a generalized technique for image enhancement and restoration. It simultaneously normalizes the brightness across an image and increases contrast. Most importantly, homomorphic filters transform multiplicative noise into additive noise using the logarithmic operator. After the image has been trans-

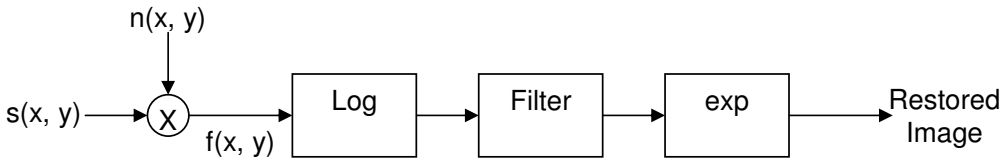

Figure 5.1: A signal flow diagram of a typical homomorphic transformation.

5.3 A Review of Gagnon's "Homomorphic Elliptical Thresholding" Algorithm

Referring to Figure 5.2, a logarithm is taken of the gray-level values of the speckle-corrupted image's pixels, thereby transforming the image into the homomorphic domain, where the speckle's multiplicative corruption of the original image becomes additive.

For each pair $\{H, H\}, \{H, V\}$ or $\{V, H\}$ at each of the N levels of wavelet-decomposition in Figure 5.2, the wavelet-coefficients' real-value and imaginary-value parts are found to be approximately bi-normal and cross-correlated on the complex-plane, with non-zero means [39]. See Figure 5.3. This motivates in [39] a

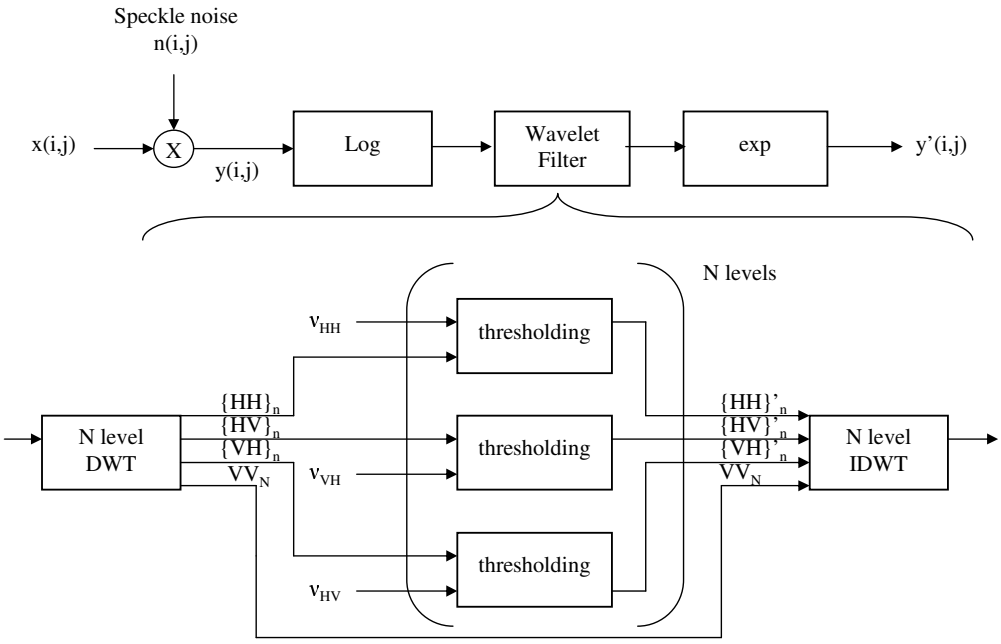

Figure 5.2: Signal flow diagram of the speckle noise suppression algorithm

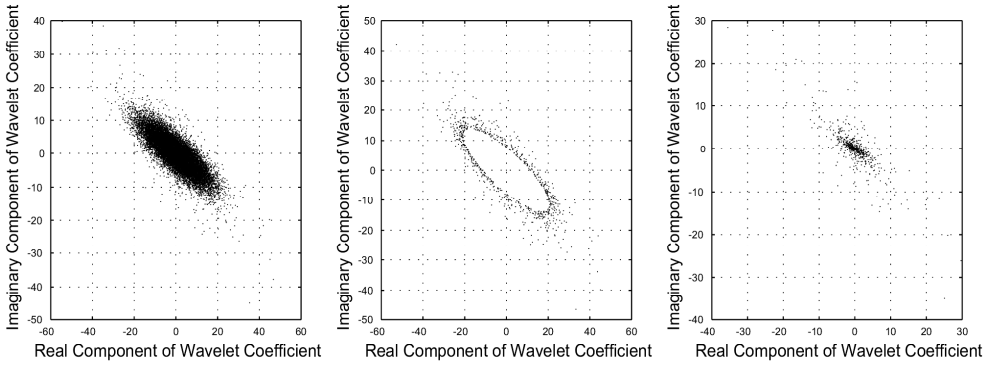

Figure 5.3: Complex wavelet coefficient distribution within the complex plane (left) elliptical hard thresholding (center) elliptical soft thresholding (right)

two-dimensional threshold consisting of an elliptical ring whose elliptical axes are aligned with the binormal distribution's orientation on the complex-plane. The orientation of the principal coordinate axes, of the ellipse formed by an image's wavelet-coefficients on the complex-plane, depends on the particular image itself and the specific choice of the wavelet basis.

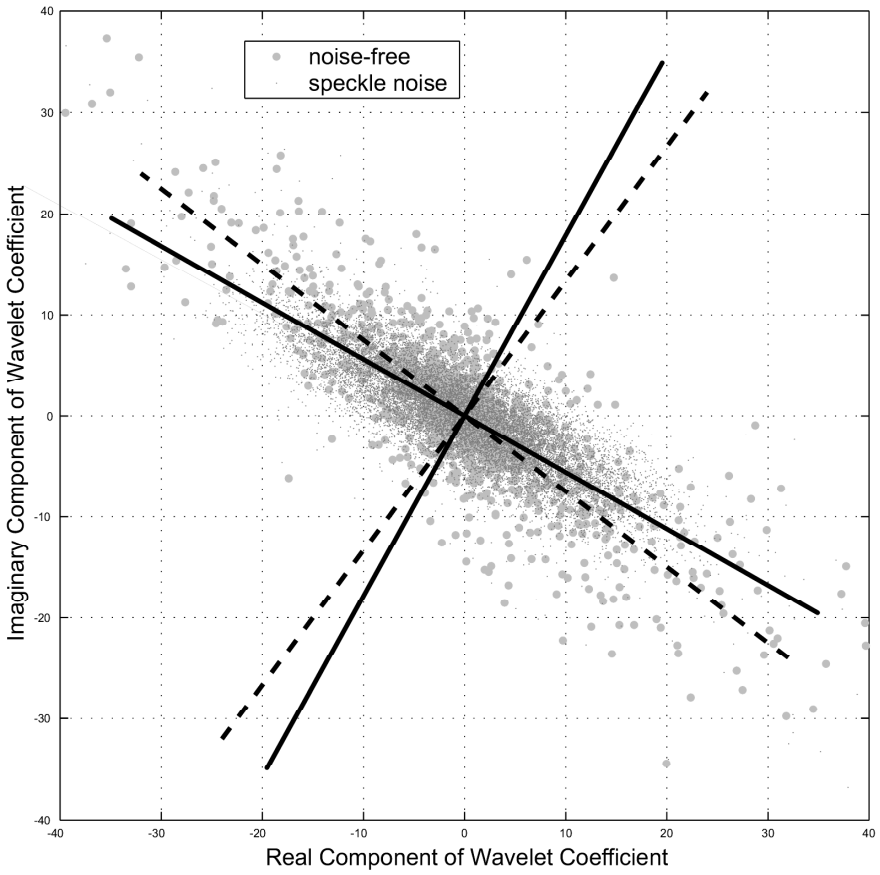

Figure 5.4: Noisy and noise-free complex wavelet coefficient distribution

Let $\mathbf{x} = \mathbf{x}^{(r)} + j\mathbf{x}^{(i)}$ represent a $Q \times 1$ vector of Q complex-value wavelet-coefficients for a particular subband. Each row in the $Q \times 2$ matrix $\mathbf{X} = \left[\mathbf{x}^{(r)} \;\; \mathbf{x}^{(i)}\right]$ lies in a two-dimensional vector-space $\mathcal{V}$. Define the 2×2 covariance matrix (or

dispersion matrix),

$$\mathbf{C_X} \;=\; \left(\mathbf{X}-\bar{\mathbf{X}}\right)^T\left(\mathbf{X}-\bar{\mathbf{X}}\right) \tag{5.1}$$

where $\bar{\mathbf{X}} = \mathbf{1}\otimes[\bar{x}^{(r)}\;\bar{x}^{(i)}]$, $\mathbf{1}$ denotes a size-compatible vector of all 1's, $\otimes$ refers to the Kronecker product, the scalar $\bar{x}^{(r)}$ equals the arithmetic mean (or centroid) of all Q entries in $\mathbf{x}^{(r)}$, and the scalar $\bar{x}^{(i)}$ likewise averages all Q entries in $\mathbf{x}^{(i)}$.

To facilitate subsequent geometric rotation of the wavelet-coefficient matrix $\mathbf{X}$ for noise reduction, translate all elements of $\mathbf{x}$ by the centroid $\bar{x} = \bar{x}^{(r)} + j\bar{x}^{(i)}$:

$$\tilde{\mathbf{x}} \;=\; \mathbf{x} - \bar{x}\mathbf{1} \tag{5.2}$$

such that the elements in $\tilde{\mathbf{x}}$, as a set, have an arithmetic center at the complex plane's origin.

To decorrelate the elements of $\tilde{\mathbf{x}} = \tilde{\mathbf{x}}^{(r)} + j\tilde{\mathbf{x}}^{(i)}$ (as a set) on the complex-plane, linear-transform $\tilde{\mathbf{X}} = [\tilde{\mathbf{x}}^{(r)}\;\;\tilde{\mathbf{x}}^{(i)}]$ into

$$\mathbf{Y} = [\mathbf{y}^{(r)}\;\;\mathbf{y}^{(i)}] = \tilde{\mathbf{X}}\mathbf{T} \tag{5.3}$$

where the 2×2 matrix $\mathbf{T}$ has 2 columns equal to the eigenvectors of $\mathbf{C_X}$. The entries of $\mathbf{y} = \mathbf{Y}[1\;\;j]^T$ turn out to distribute roughly elliptical [39] with respect to the new Cartesian axes defined by the 2 columns of $\mathbf{T}$. These two orthogonal axes forms the aforementioned ellipse's principal axes [39].

Complex-phase-dependent thresholding may be realized with respect to this ellipse's principal axes. To perform complex-phase-dependent thresholding, a sep-

arate ellipse can specify the threshold boundary at each spectral subband [39]:

$$\delta(\theta) \;=\; \frac{ab}{\sqrt{(a\sin\theta)^2+(b\cos\theta)^2}} \tag{5.4}$$

where θ represents the polar-coordinate angle on $\mathcal{V}_c$, $a=\nu\sigma^{(r)}$ symbolizes the elliptical threshold's major-axis' length, and $b=\nu\sigma^{(i)}$ represents the elliptical threshold's minor-axis' length, $\sigma^{(r)}$ refers to the arithmetic standard deviation among the entries in $\mathbf{y}^{(r)}$, $\sigma^{(i)}$ symbolizes the arithmetic standard deviation among the entries in $\mathbf{y}^{(i)}$, ν is a deign parameter to be specified for this denoising algorithm and will be used to implicitly define a new rotation matrix from $\mathcal{V}_c$ back to $\mathcal{V}$.

Expressing the qth entry in $\mathbf{y}$ in polar coordinates as $y_q = y_q^{(\rho)}e^{jy_q^{(\theta)}}$, hard-thresholding may be realized as follows:

$$\tilde{y}_q \;=\; t_{\text{hard}}(y_q^{(\rho)},\delta(y_q^{(\theta)})) = \begin{cases} 0, & y_q^{(\rho)} \le \delta(y_q^{(\theta)}) \\ y_q, & \text{otherwise} \end{cases} \tag{5.5}$$

Soft-thresholding may be realized as:

$$\tilde{y}_q \;= t_{\text{soft}}(y_q^{(\rho)},\delta(y_q^{(\theta)})) = \max\left(0, y_q^{(\rho)}-\delta(y_q^{(\theta)})\right)e^{jy_q^{(\theta)}} \tag{5.6}$$

Hard-thresholding is algorithmically simpler, but the noise-dominated wavelet-coefficients may pass the hard-threshold to appear as annoying "blips" which, however, can be diminished by soft-thresholding [22].

A "universal threshold" $\delta_{\text{universal}}$ has been derived in [36] as asymptotically optimal for a $Q\times R$ signal-matrix with a noise variance σ_{noise},

$$\delta_{\text{universal}} \;=\; \sqrt{2QR\log(QR)\sigma_{\text{noise}}} \tag{5.7}$$

Setting the right-hand side of (5.4) to equal the pre-computed right-hand side of (5.7), ν may be computed and the "homomorphic elliptical thresholding" algorithm is tuned for use.

5.4 The "Rotated Elliptical Thresholding" Algorithm

5.4.1 Type I Filtering

When an image becomes speckled, the corrupted image's homomorphic-domain's wavelet-coefficients' elliptical axes rotate from those of the original image [39]. Hence, this work proposes a counter-rotation of the corrupted-image's elliptical axes as a denoising strategy. [2] See Figure 5.4. Because the large-magnitude wavelet-coefficients are usually less sensitive to noise [22], the remaining wavelet-coefficients are rotated on the complex-plane to increase noise reduction.

Define

$$\tilde{x}_q \;=\; \begin{cases} x_q, & \text{if } \tilde{y}_q > 0 \\ 0, & \text{if } \tilde{y}_q \leq 0 \end{cases} \tag{5.8}$$

Further define the qth row of the $Q \times 2$ matrix $\tilde{\mathbf{X}}$ to equal $[\mathrm{Re}(\tilde{x}_q),\ \mathrm{Im}(\tilde{x}_q)]$. Then, form a new 2×2 counter-rotation transformation matrix $\tilde{\mathbf{T}}$, whose columns equal the eigenvectors of $\mathbf{C}_{\tilde{\mathbf{x}}} = \tilde{\mathbf{X}}\tilde{\mathbf{X}}^H$ to map from $\mathcal{V}_c$ to a new space $\mathcal{V}_s$. While $\mathbf{T}$ regularizes the homomorphic noisy image's translated wavelet-coefficients, $\tilde{\mathbf{T}}_s$ counter-regularize the translated-regularized-thresholded wavelet-coefficients of the homo-

[2] The authors' simulation results suggest that this noise-induced axes-rotation is especially significant on the first decomposition level.

morphic noisy image. In $\mathcal{V}_s$ (defined by successive application of $\boldsymbol{T}$ and $\tilde{\mathbf{T}}$ to $\mathcal{V}_c$), the translated-regularized-threshold-counterregularized wavelet-coefficients constitute the elements of $\mathbf{x}_s = \mathbf{X}_s[1 \quad j]^T$, where

$$\mathbf{X}_s \;=\; \tilde{\mathbf{Y}}\tilde{\mathbf{T}}^T \tag{5.9}$$

If no speckle were present, $\tilde{\mathbf{X}} = \mathbf{X}$ and $\mathbf{C}_{\tilde{\mathbf{x}}} = \mathbf{C}_{\mathbf{x}}$. That $\mathbf{C}_{\tilde{\mathbf{x}}} \neq \mathbf{C}_{\mathbf{x}}$ is entirely due to the speckle and the preceding mitigation steps. The noiseless image can thus be obtained by a counter-rotation and counter-translation defined by $\mathbf{C}_{\tilde{\mathbf{x}}}$.

With the earlier mitigation steps, $\mathbf{x}_s = \mathbf{x}_s^{(r)} + j\mathbf{x}_s^{(i)}$ would ideally be free of speckle. Hence, the denoised image may be obtained by inverse-wavelet-transforming by counter-translating and then inverse-wavelet-transforming $\mathbf{x}_s$. Thus, counter-translate the elements of $\mathbf{x}_s$ by the centroid $\bar{x}$,

$$\hat{\mathbf{s}} \;=\; \mathbf{x}_s + \bar{x}\mathbf{1} \tag{5.10}$$

Inverse-wavelet-transform $\hat{\mathbf{s}}$ to obtained the denoised image. Any non-zero imaginary value from the inverse-wavelet transformation is set to zero. The real part is normalized to within $[0, 255]$ and rounded to $\{0, \cdots, 255\}$.

5.4.2 Type II Filtering

One disadvantage of the type I filter is its lack of shift invariance. As a result, wavelet decomposition of a signal differs when the signal is shifted by one data point. Of course, this can modify the noise estimate in the algorithm by using the DT CWT discussed in section 4.5.

Modifications to the type I filter algorithm are slight, as each subband coefficient

distribution is denoised identically. With the added directional selectivity offered by the dual tree complex wavelet transform, there are six subbands per level, implying that twice as much processing is required and twice the number of parameters are necessary. The type II filter should provide greater stability and edge sensitivity in the noise reduction process compared to type I filters. The main drawback is the additional computations required for analysis.

5.5 Summary

This chapter discussed the elliptical noise reduction algorithms, type 1 and type 2. In the next chapter we interpret images denoised using the ETR algorithm and compares the results to various standard filters.

Chapter 6

Speckle Noise Suppression Simulation Results and Analysis

For the evaluation of the performance of the speckle reductions filters, we set up the following measurement principles:

1. A good filter should maintain the average mean of an image. It is measured by the bias factor.

2. The ability of a filter to reduce the speckle. It is evaluated by the ENL (Equivalent Number of Looks) factor and the S/MSE ratio. The ENL factor is related to the resolution of the image. The S/MSE is an estimate of the signal to noise content.

Experiments and simulations were carried out for the proposed algorithms using different images categorized into 5 different areas using real and simulated data:

1. Angular Structures

2. Curve Structures

3. Homogeneous Areas

4. Linear Structures

5. local structures

The following sections address the performance of the proposed algorithm with the standard filters and investigate the general wavelet filter performance.

6.1 Angular Structure

Like the local targets and edges, a sharp angle of an object will be blurred by filters. In this experiment, the filters are tested for the ability of preserving the angular structures of an image. Figure 6.1 shows the ability of the filters in preserving the angular structures.

Figure 6.2 shows clinical images containing various angular structures. The clinical images are harder to decipher due to the large black back ground but the wavelet images have advantages particular in the corner regions. Type II filters have this property most clearly.

Table 6.1 shows the numerical values of the noise reduction indicators. In this image, the test image shows that the wavelet filters have a better S/MSE ratio and ENL values. The clinical images also reveal the same conclusion. The wavelet filter's ability to smooth noise and retain edges contribute to its superior improvement over traditional filters.

(a) Original Image

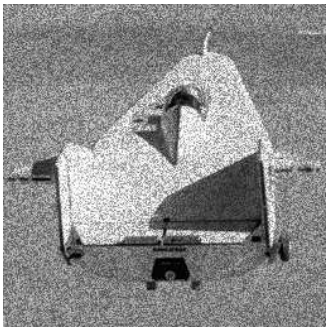

(b) Speckle Image

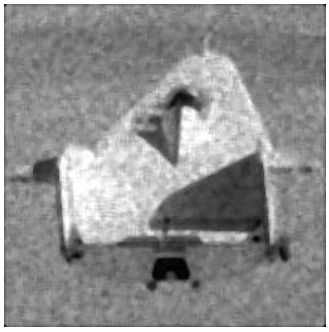

(c) Median Filtered Image

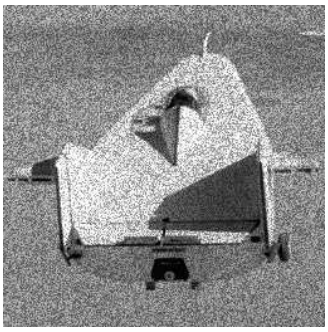

(d) Statistic Lee Filtered Image

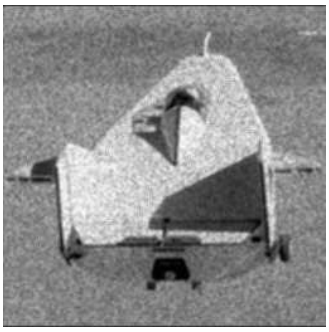

(e) Kuan Filtered Image

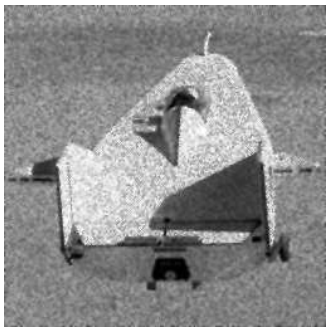

(f) Enhanced Frost Filtered Image

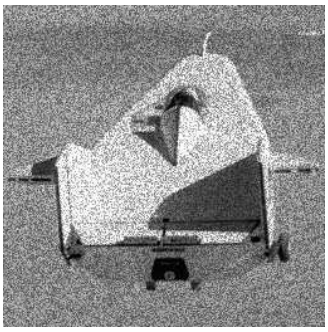

(g) Gamma Filtered Image

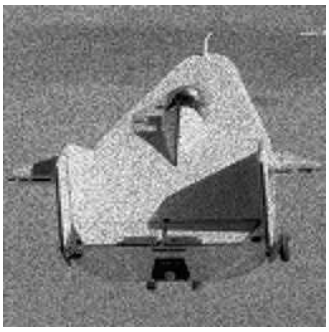

(h) Proposed Scheme's Denoised Image (type 1)

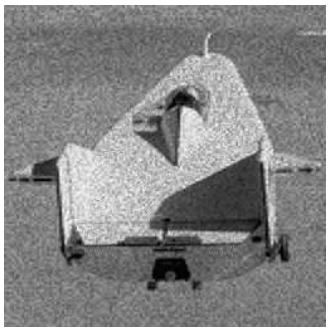

(i) Proposed Scheme's Denoised Image (type 2)

Figure 6.1: Angular Structure Simulation Results using Standard Images

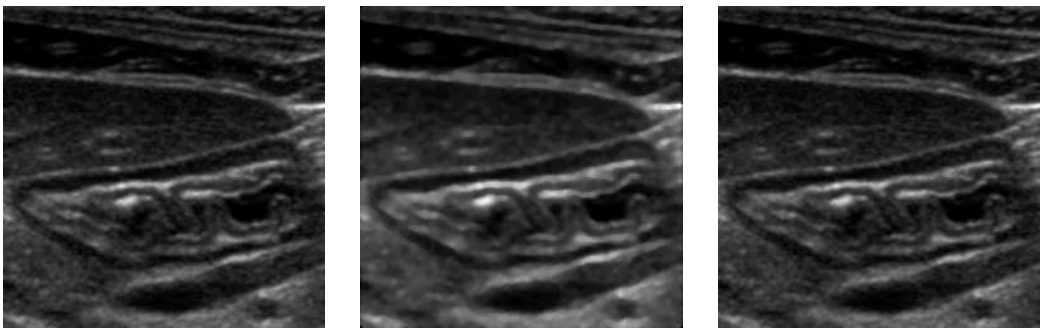

(a) Given Noisy Image (b) Median Filtered (c) Statistic Lee Filtered Image

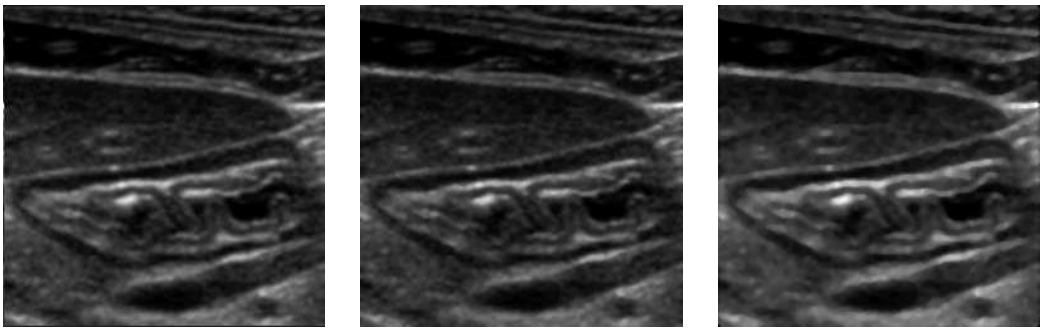

(d) Kuan Filtered Image (e) Enhanced Frost Filtered Image (f) Gamma Filtered Image

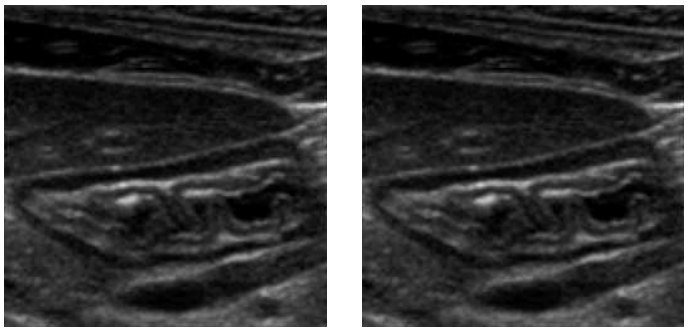

(g) Proposed Scheme's Denoised Image (type 1) (h) Proposed Scheme's Denoised Image (type 2)

Figure 6.2: Comparing various de-speckling approaches using a clinically speckled ultrasound image of angular structures.

Table 6.1: Summary of Speckle Noise Reduction for Angular Images. Note: The S/MSE value cannot be calculated for ultrasound images as the original is not available for comparison.

Filter	**Test Image**, $\sigma_N = 0.05$		**Ultrasound Image**	
	S/MSE (dB)	ENL	S/MSE (dB)	ENL
Noisy	13.4779	7.0694	-	2.0127
Median	19.7638	9.9872	-	2.2253
Lee	13.5025	7.1014	-	2.0127
Kuan	20.3170	10.5270	-	2.1566
Frost	20.0006	10.3156	-	2.1297
Gamma	13.4096	7.0688	-	1.8328
Wavelet (type I)	20.5009	11.0667	-	2.0856
Wavelet (type II)	22.2900	12.4939	-	2.6855

6.2 Curve Structure

In Figure 6.3, speckle noise is added to an uncorrupted MRI image; and the resulting image's pixel magnitudes are normalized and rounded to $\{0, \cdots, 255\}$. This corrupted image is denoised using the proposed algorithm with soft thresholding, median filtering and homomorphic adaptive Wiener filtering. Visual qualitative assessment suggests that relative to the proposed algorithm, the latter two customary algorithms offer worse speckle-suppression and loose more signal details, excessively blurring the denoised images.

Figure 6.4 shows a clinically speckled ultrasound image denoised using the proposed algorithm with soft thresholding, and other filtering strategies. Where required, a 7×7 mask is used. Visual qualitative assessment suggests that relative to the proposed algorithm, the latter customary algorithms offer worse speckle-suppression and lose more signal details to excessively blur the denoised images.

Table 6.2 shows the numerical values of the noise reduction indicators. The

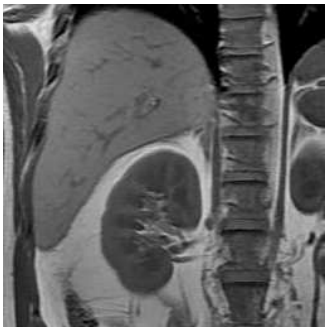

(a) Original Image

(b) Speckle Image

(c) Median Filtered Image

(d) Statistic Lee Filtered Image

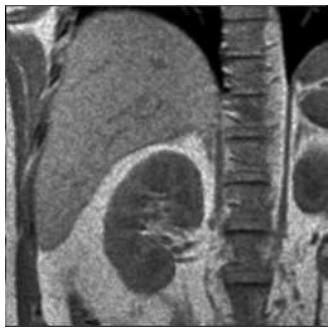

(e) Kuan Filtered Image

(f) Enhanced Frost Filtered Image

(g) Gamma Filtered Image

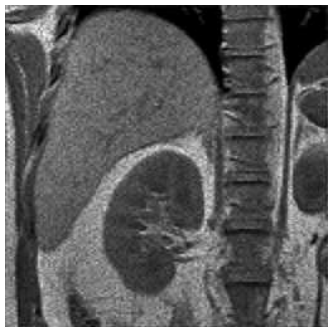

(h) Proposed Scheme's Denoised Image (type 1)

(i) Proposed Scheme's Denoised Image (type 2)

Figure 6.3: Curve Structure Simulation Results using Standard Images

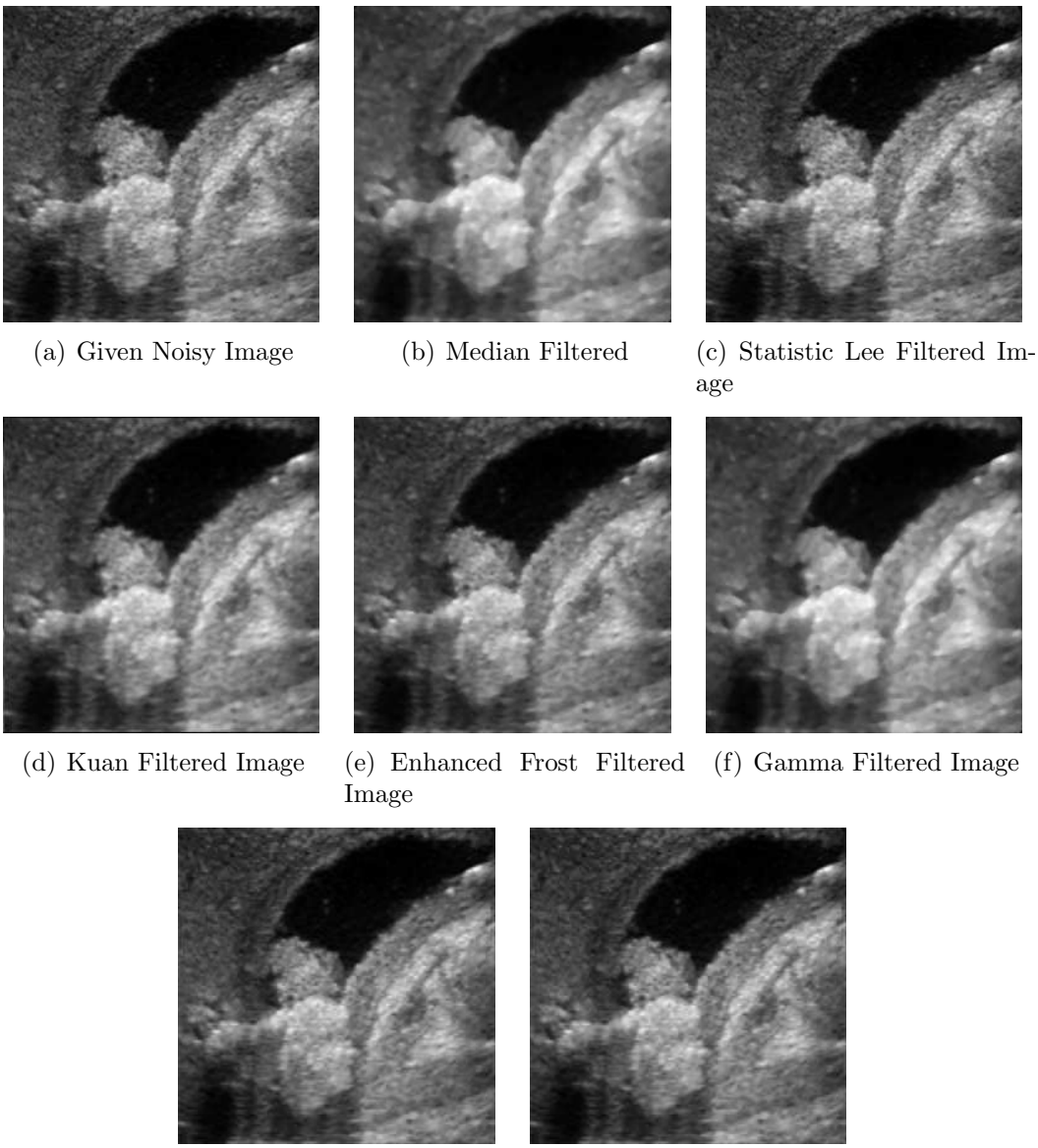

(a) Given Noisy Image (b) Median Filtered (c) Statistic Lee Filtered Image

(d) Kuan Filtered Image (e) Enhanced Frost Filtered Image (f) Gamma Filtered Image

(g) Proposed Scheme's Denoised Image (type 1) (h) Proposed Scheme's Denoised Image (type 2)

Figure 6.4: Comparing various de-speckling approaches using a clinically speckled ultrasound image of curve structures.

Table 6.2: Summary of Speckle Noise Reduction for Curvy Images. Note: The S/MSE value cannot be calculated for ultrasound images as the original is not available for comparison.

Filter	**Test Image**, $\sigma_N = 0.05$		**Ultrasound Image**	
	S/MSE (dB)	ENL	S/MSE (dB)	ENL
Noisy	13.0279	4.0545	-	2.6358
Median	18.1196	5.6824	-	2.7077
Lee	13.0206	4.0612	-	2.6366
Kuan	18.8602	5.5997	-	2.6607
Frost	18.7260	5.1997	-	2.6930
Gamma	12.9750	4.0368	-	2.2701
Wavelet (type I)	18.5064	5.1880	-	2.6817
Wavelet (type II)	19.5727	5.3167	-	2.9811

wavelet filters offer slightly better ratios than the median, kuan, and frost filters as well as improved ENL ratios.

6.3 Homogeneous Areas

Figure 6.5 shows the various standard filters in comparison to the elliptical rotational thresholding algorithm proposed in this thesis for a generally homogenous image of the earth's moon. The images show that the wavelet filter's superior performance, as the craters present in the lower left hand corner which were not well preserved in the other images.

Figure 6.6 shows reduction of homogeneous regions on an ultrasound image. The median filter shows very poor results due to over-smoothing while the lee filter tends to under-smooth images.

Table 6.3 shows the numerical values of the noise reduction indicators. In this

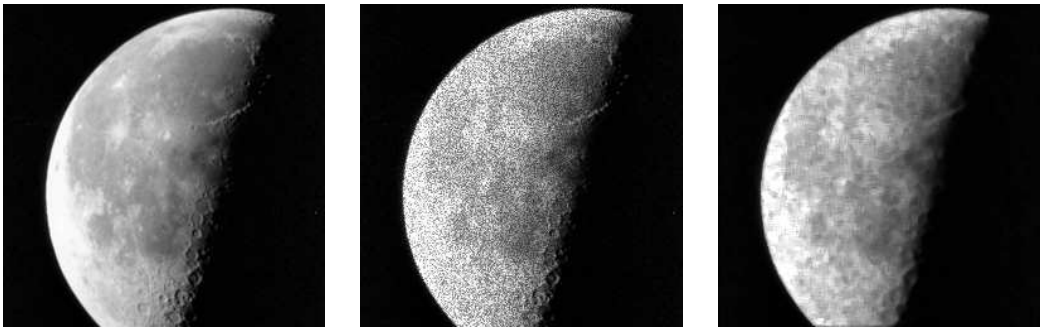

(a) Original Image (b) Speckle Image (c) Median Filtered Image

(d) Statistic Lee Filtered Image (e) Kuan Filtered Image (f) Enhanced Frost Filtered Image

(g) Gamma Filtered Image (h) Proposed Scheme's Denoised Image (type 1) (i) Proposed Scheme's Denoised Image (type 2)

Figure 6.5: Homogeneous Area Simulation Results using Standard Images

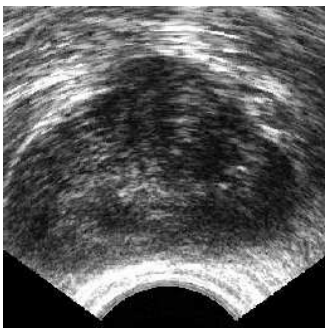

(a) Given Noisy Image

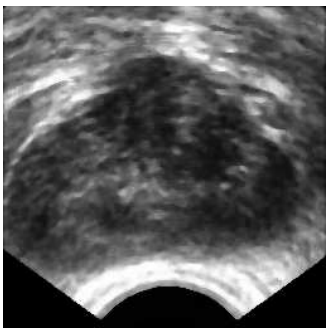

(b) Median Filtered

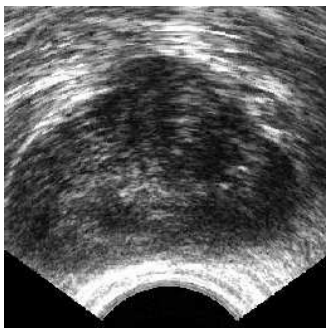

(c) Statistic Lee Filtered Image

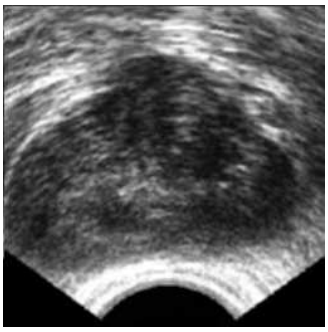

(d) Kuan Filtered Image

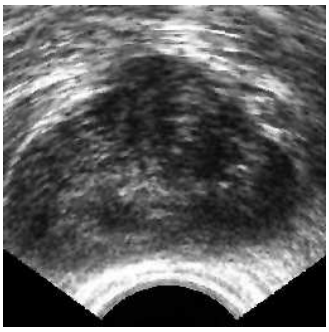

(e) Enhanced Frost Filtered Image

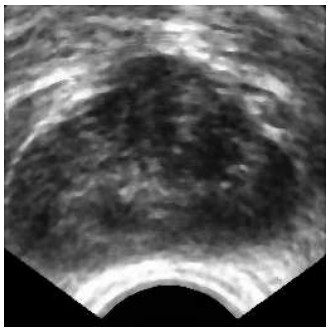

(f) Gamma Filtered Image

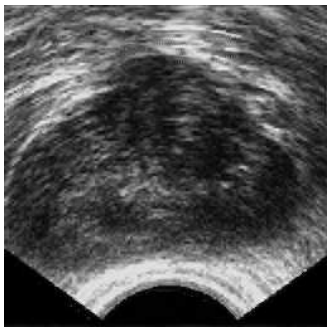

(g) Proposed Scheme's Denoised Image (type 1)

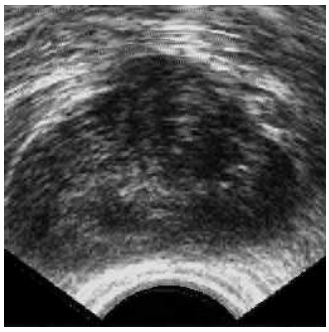

(h) Proposed Scheme's Denoised Image (type 2)

Figure 6.6: Homogeneous Area Simulation Results using Ultrasound Images

Table 6.3: Summary of Speckle Noise Reduction for Homogeneous Images. Note: The S/MSE value cannot be calculated for ultrasound images as the original is not available for comparison.

Filter	**Test Image**, $\sigma_N = 0.05$		**Ultrasound Image**	
	S/MSE (dB)	ENL	S/MSE (dB)	ENL
Noisy	13.7189	0.7231	-	1.7490
Median	20.8743	0.7528	-	1.8916
Lee	13.6962	0.7234	-	1.7490
Kuan	20.0826	0.7780	-	1.9416
Frost	17.1429	0.7577	-	1.8819
Gamma	13.3671	0.7140	-	1.7039
Wavelet (type I)	15.7274	0.7957	-	1.9022
Wavelet (type II)	18.9716	0.8086	-	2.0860

instant, the Kuan filter showed the best results in terms of numerical values with the median filter. However, the images show that the kuan filter do not have good resolution near the edges. This result is due to the large homogeneous regions, causing filters that tend to smooth images to perform slightly better than others.

6.4 Linear Structure

Patterns were also used to test these speckle filters. Figure 6.7 shows the speckled image filtered by using the aforementioned filters, all with window size of 7x7 pixels and K=l for the Enhanced Frost filters. From these filtered images, it is observed that, in terms of preservation of linear features, the best one is the Frost filter. This is expected since from the test of edges, it is seen that the Frost filter has the best ability to preserve edges. However, the Frost filter (K=l) does not have a good ability of reducing the speckles. It is interesting to note that the linear features of the sub-images in the first column (dark lines) are destroyed more than that in the

Table 6.4: Summary of Speckle Noise Reduction for Linear Images. Note: The S/MSE value cannot be calculated for ultrasound images as the original is not available for comparison.

Filter	**Test Image**, $\sigma_N = 0.05$		**Ultrasound Image**	
	S/MSE (dB)	ENL	S/MSE (dB)	ENL
Noisy	13.0670	2.9347	-	3.3485
Median	16.3257	3.5559	-	3.4660
Lee	13.1036	2.9426	-	3.3485
Kuan	17.4337	3.7660	-	3.4643
Frost	18.9843	3.6222	-	3.4395
Gamma	13.0107	2.8738	-	3.0623
Wavelet (type I)	18.3028	3.5639	-	3.4643
Wavelet (type II)	19.7483	3.6589	-	3.5739

first row (bright lines). This is because of the multiplicative feature of the speckle. That is, the brighter the pixels are, the more the speckle effects.

Figure 6.8 shows speckle noise reduction on an ultrasound image with linear structures. This image is difficult to interpret due to the large amount of black present. As the eye is not accustomed to contrast within darker regions, the improvements are not as evident and we need to fall back on the numerical analysis to provide an indication for the speckle noise reduction effectiveness.

Table 6.4 shows the numerical values of the noise reduction indicators. Overall, the Frost and wavelet filters produced the best S/MSE values, with the ENL vlaues showing similar results. The ENL value calculated over the whole ultrasound image also sows improvement via the suggested techniques. Although the wavelet filter is not evidently superior in this case, the customary filters also perform similarly.

(a) Original Image

(b) Speckle Image

(c) Median Filtered Image

(d) Statistic Lee Filtered Image

(e) Kuan Filtered Image

(f) Enhanced Frost Filtered Image

(g) Gamma Filtered Image

(h) Proposed Scheme's Denoised Image (type 1)

(i) Proposed Scheme's Denoised Image (type 2)

Figure 6.7: Linear Structure Simulation Results using Standard Images

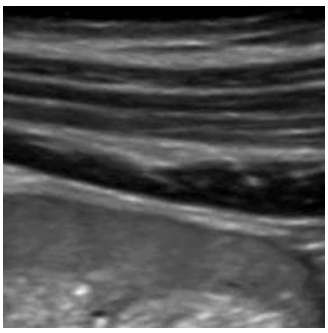

(a) Given Noisy Image

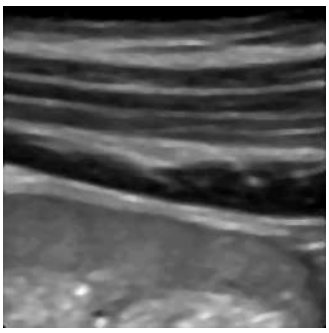

(b) Median Filtered

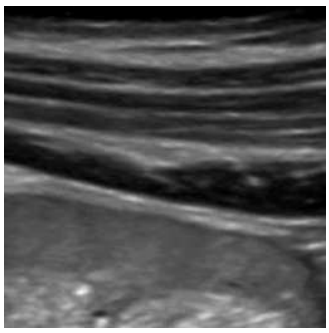

(c) Statistic Lee Filtered Image

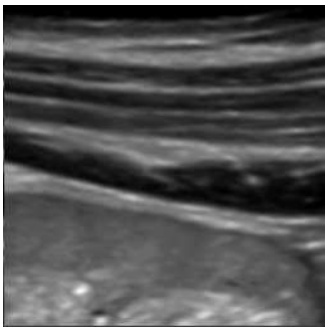

(d) Kuan Filtered Image

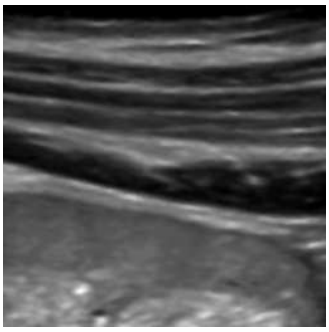

(e) Enhanced Frost Filtered Image

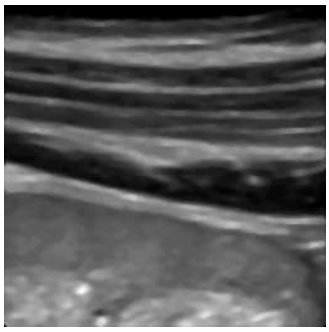

(f) Gamma Filtered Image

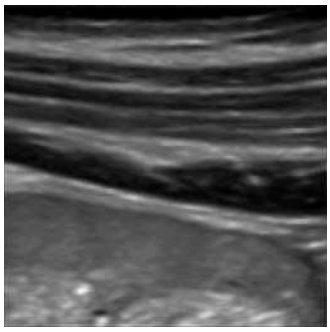

(g) Proposed Scheme's Denoised Image (type 1)

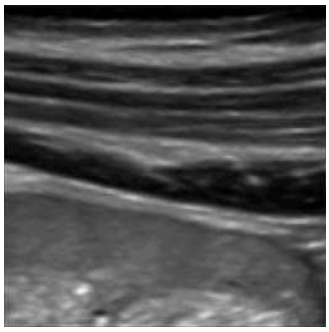

(h) Proposed Scheme's Denoised Image (type 2)

Figure 6.8: Comparing various de-speckling approaches using a clinically speckled ultrasound image of linear structures.

6.5 local structure

Figure 6.9 shows an experiment where the filters are tested on local targets. The noisy image was created artificially using a noise variance of 0.05 following the fully blown speckle statistics described in Chapter 2.

The following filters were tested: Median, the Lee, the Kuan, the Enhanced Frost, the Gamma MAP, and the type I and type II proposed wavelet filters. The window size is of 7×7 pixels and K=l for the Enhanced Frost filters. The optimal wavelet filters were found by a .1 grid exhaustive search in which each subband was varied identically. It has been found that the median filter smooths out the local targets as expected. The other filters retain the local target after filtering. However, due to the upper bound used in the Enhanced Frost and the Gamma MAP filters, these three filters do not reduce the speckles of the local target and its surrounding area. In contrast, the Lee, the Kuan and the Frost filters not only smooth out the speckle on the homogeneous area but also the speckle on the local target. Overall, the wavelet filters were able to retain the targets and perform smoothing in homogeneous regions.

Similar results can be found in figure 6.10, showing the clinical images where with various local structures present. A clear superior image for the wavelet filters are found by observing this set as the details of the thyroid are evident without blurring of the edges.

Table 6.5 shows the numerical values of the noise reduction indicators. Overall, the results confirm the visual analysis. The Median, Frost, and Wavelet filters achieved high scores for the S/MSE and ENL values. However, as can be noted, some filters such as the median image looks poor but have good numerical values. Therefore, the values should be taken in conjunction to the images presented.

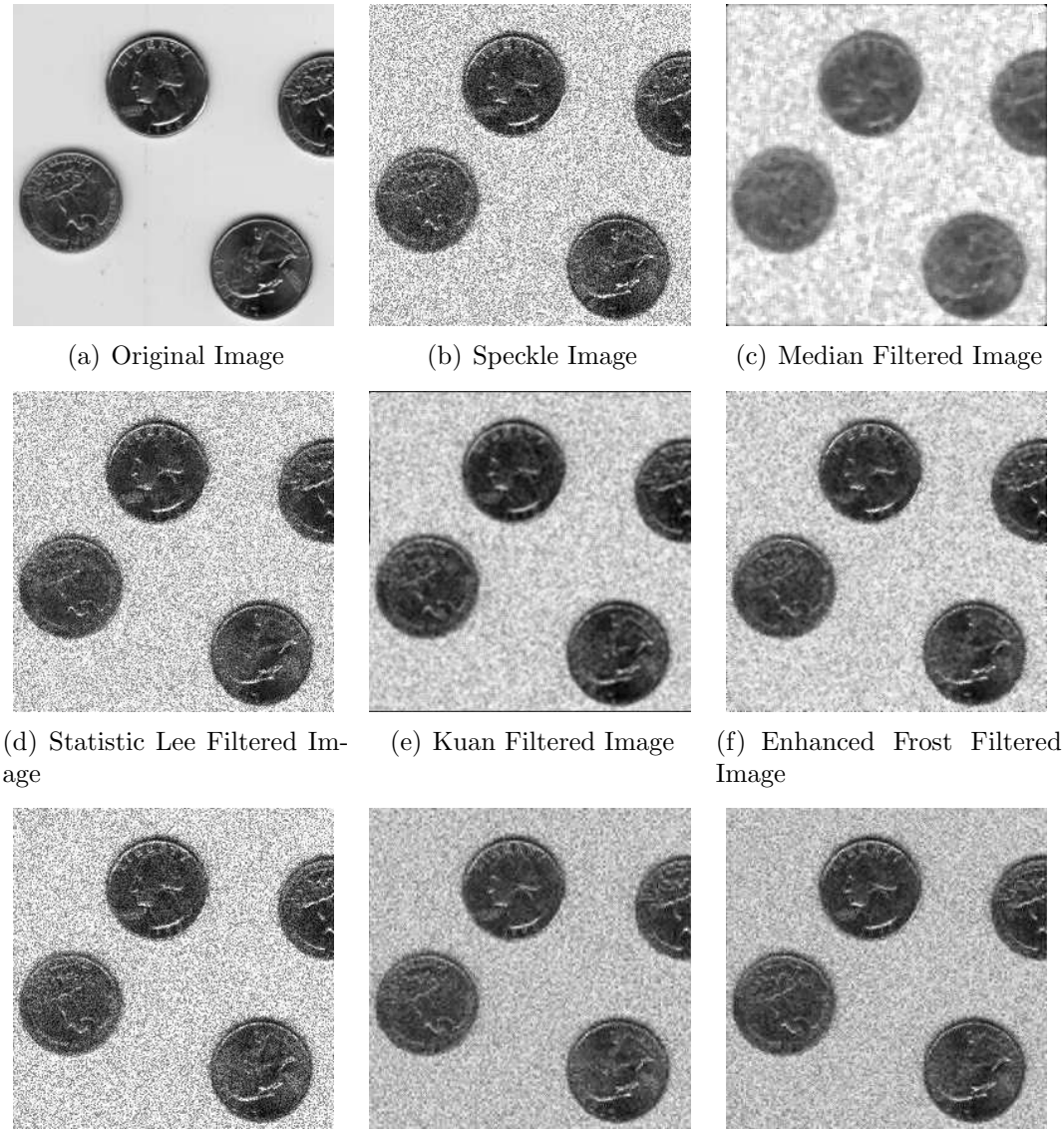

(a) Original Image (b) Speckle Image (c) Median Filtered Image

(d) Statistic Lee Filtered Image (e) Kuan Filtered Image (f) Enhanced Frost Filtered Image

(g) Gamma Filtered Image (h) Proposed Scheme's Denoised Image (type 1) (i) Proposed Scheme's Denoised Image (type 2)

Figure 6.9: local structure Simulation Results using Standard Images

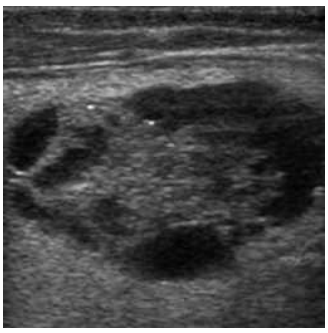

(a) Given Noisy Image

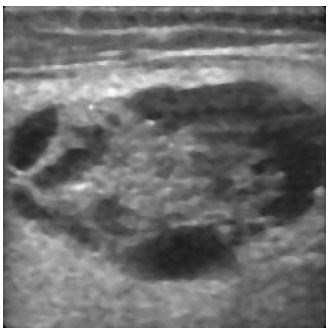

(b) Median Filtered

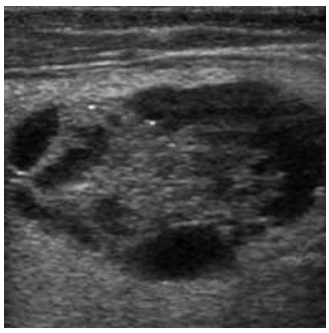

(c) Statistic Lee Filtered Image

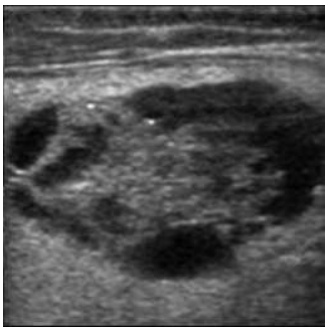

(d) Kuan Filtered Image

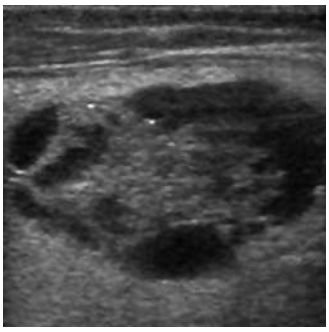

(e) Enhanced Frost Filtered Image

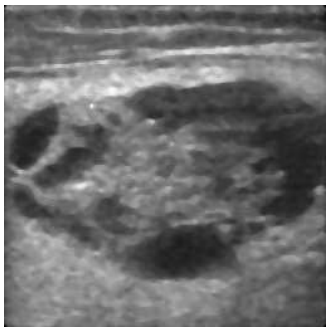

(f) Gamma Filtered Image

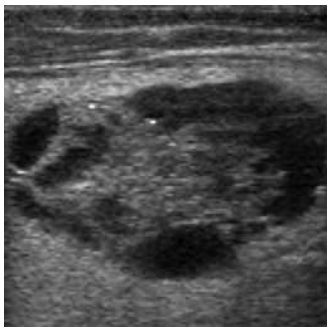

(g) Proposed Scheme's Denoised Image (type 1)

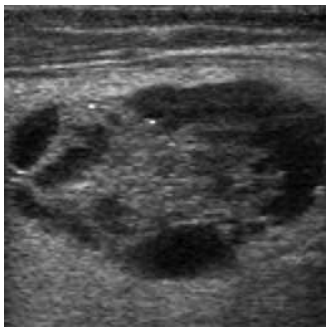

(h) Proposed Scheme's Denoised Image (type 2)

Figure 6.10: local structure Simulation Results using Ultrasound Images

Table 6.5: Summary of Speckle Noise Reduction for local structure Images. Note: The S/MSE value cannot be calculated for ultrasound images as the original is not available for comparison.

Filter	**Test Image**, $\sigma_N = 0.05$		**Ultrasound Image**	
	S/MSE (dB)	ENL	S/MSE (dB)	ENL
Noisy	14.7323	8.5259	-	3.3485
Median	20.3380	10.7024	-	3.4660
Lee	15.6813	9.2663	-	3.3485
Kuan	19.6316	11.9598	-	3.4643
Frost	21.0623	12.0116	-	3.4395
Gamma	14.6476	8.5282	-	3.0623
Wavelet (type I)	19.3176	11.5711	-	3.4643
Wavelet (type II)	20.4985	11.3155	-	3.5739

6.6 Analysis of the Wavelet Filter Performance

A numerical analysis was conducted about the behavior of the ETR filter over a change (1) in the wavelet coefficient thresholding type (soft- versus hard thresholding) and (2) in the variation of the filter parameters. This provides much information on the optimal application range of the filter in practical situations. All subsequent simulations use the $N = 6$th-order complex Daubechies wavelet[1]. For all subsequent figures, the original noiseless image $\{s_{i,j}\}$ has 256×256 pixels with 256 possible gray-levels. Speckled noise $\{n_{i,j}\}$ produces a speckled-image with pixels $x_{i,j} = \mathrm{F}\left([1 + n_{i,j}]s_{i,j}\right)$, where $\{n_{i,j}\}$ is spatially uncorrelated and uniformly distributed over $[-\sqrt{3}/5, \sqrt{3}/5]$ with a 0 mean and a 0.04 variance. F(.) denotes clipping and truncation to an integer in $\{0, \ldots, 255\}$. Appendix A shows the GUI designed to help identify the optimal S/MSE ratio.

Soft-thresholding scheme turns out to always give slightly better S/MSE than

[1]Although the symmetric-wavelet's order's influence is not investigated; however, higher orders do not significant enhance the visual performance [39].

hard-thresholding. Figure 6.11 shows that soft-thresholding generally offers a higher S/MSE ratio than hard-thresholding. The analysis was completed on a 256 × 256 image and has various bumps due to the lack of averaging present. However, the general trend exists. The decomposition level is limited by the size of the image [39] and for a 256 × 256 image, that value is a 2nd level decomposition.

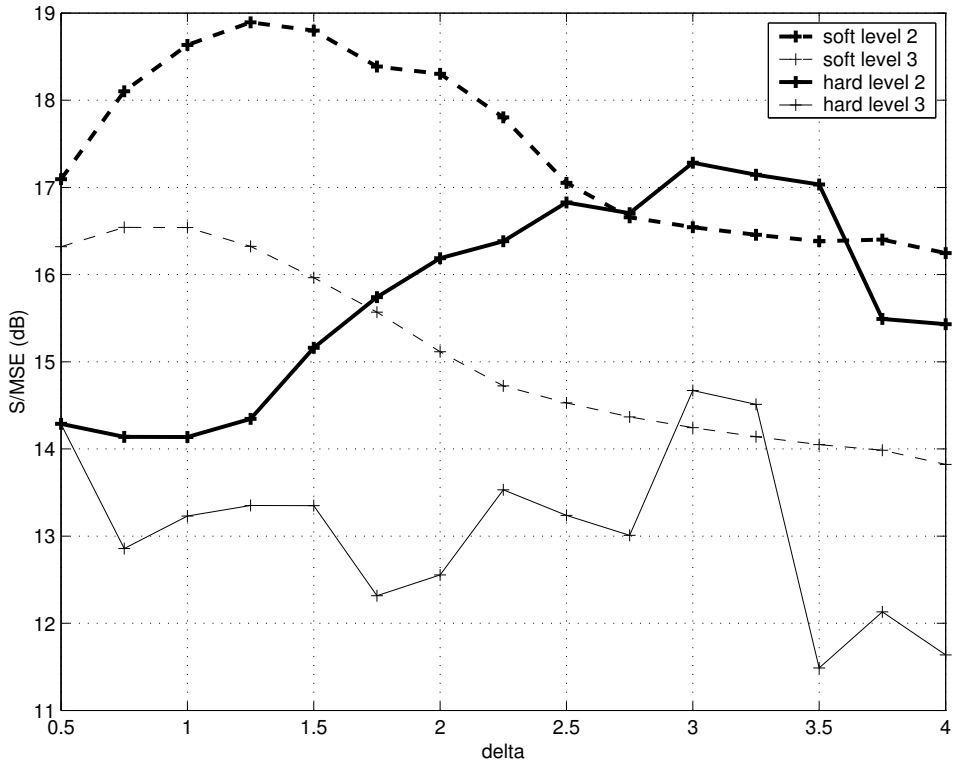

Figure 6.11: The performance of the proposed wavelet method using soft and hard thresholding

Figure 6.12 and 6.13 shows the variation of the S/MSE ratio for a soft-thresholding scheme for 4 decomposition levels, as function of the threshold parameter. Figure 6.12 shows the proposed algorithm as a function of thresholds in different wavebands via soft thresholding. Figure 6.13 shows the proposed algorithm as a func-

tion of different thresholding wavebands using a hard thresholding strategy. One also observes in Figure 6.12 and 6.13 that there is an optimal value for the threshold above which the S/MSE starts decreasing because of the oversmoothing of the image. The position of the optimal S/MSE depends on the wavelet and on the number of decomposition levels. The images shows that the experimental optimal threshold level depends on the frequency content of the image. Although [27] uses standard-deviation values from the first decomposition level for all higher levels of the wavelet-decomposition, the present authors' experimental results in Figure 6.13 seem to favor defining a new threshold for each wavelet-decomposition level, where the design-parameters ν_{HV}, ν_{VH}, and ν_{HH} respectively dictate the noise-reduction amount in the subbands HV, VH, HH. That is, "Wavelet Coefficient Shrinkage" may be applied independently to the image's three wavelet-transformed spectral bands of HV, VH, HH. In Figure 6.13, only one of these three may vary from a pre-set value of 2. Similar S/MSE is obtained by varying ν_{HV} as by varying ν_{VH}; this is expected from the symmetry between HV and VH with respect to the original image. Moreover, the highest S/MSE is obtained for this particular image when $\nu_{HH} < \nu_{HV}$ and $\nu_{HH} < \nu_{VH}$.

6.7 Summary Statistics and Analysis

Based on the above images and statistics, we can conclude the following:

- The proposed wavelet filters shows the best performance overall in terms of S/MSE values, ENL, and visual performance, particularly in cases of edge preservation and smoothing.
- The performance of the Kuan, Enhanced Frost is quite similar

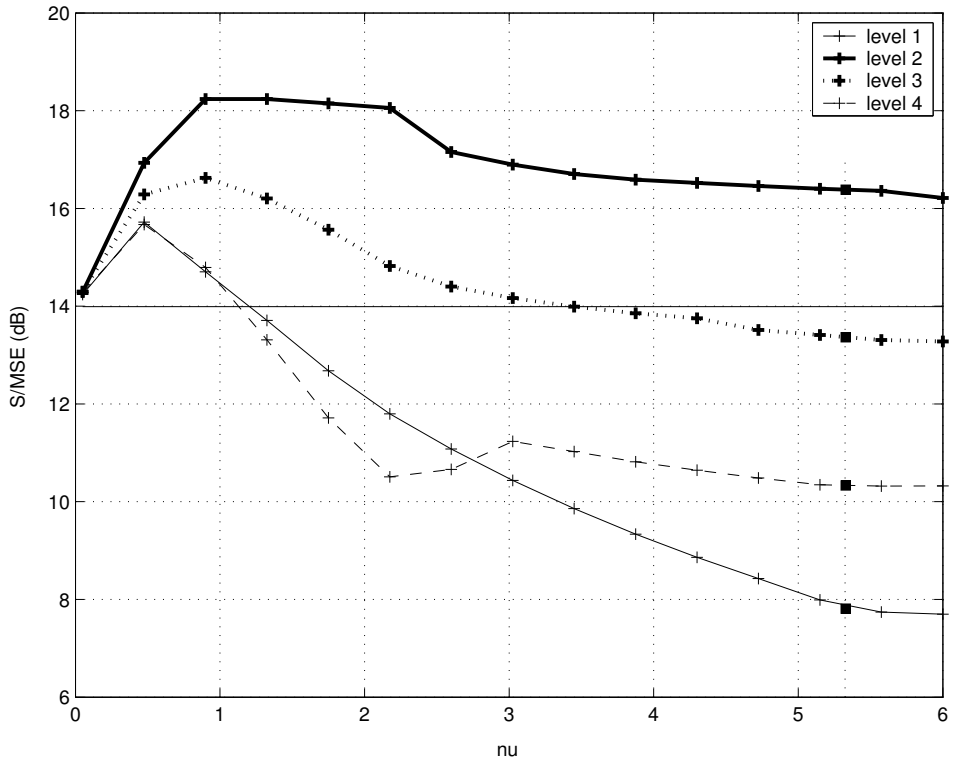

Figure 6.12: The performance of the proposed scheme (with hard thresholding) as a function of ν, with the subbands HV, VH, HH identically thresholded.

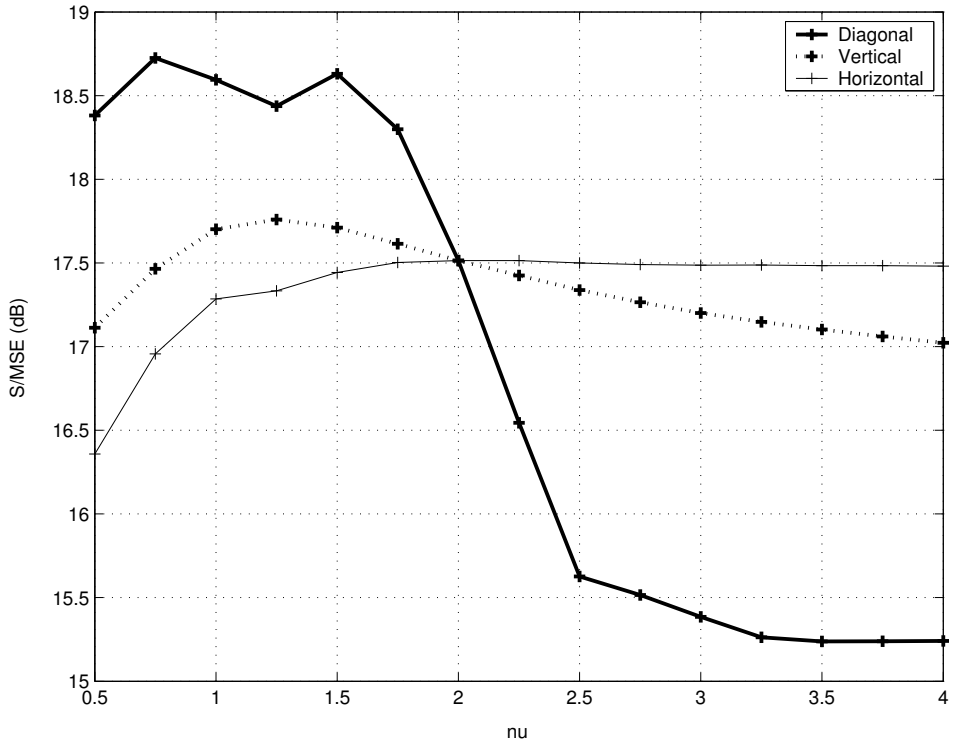

Figure 6.13: The performance of the proposed scheme (with hard thresholding) as a function of ν, with the subbands HV, VH, HH independently thresholded.

- The lee filter and median filter performed the poorest based on visual comparison and numerical analysis.

In general, all filters have a very good ability to smooth out the noise. However, it can seen that only certain filters retain edges correctly.

The best quantitative performance measures for the Median, Kuan, Frost, Wiener, Gamma and ETR filters have been analyzed. Image intensity has been preserved by assuring that the enhanced and noisy images have the same global mean. Overall, the best S/MSE is provided by the complex wavelet filter with a soft-thresholding scheme. In all cases, the ETR filter outperforms the standard ones, and especially for the low spectral content image with high level noise.

From Figure 6.14, the proposed scheme (with soft thresholding) offers a S/MSE ratio higher than customary standard filters. The results suggest that the new technique has a large potential in assisting segmentation techniques and automated area/volume calculation methods due to its superior filter performance. In general, we find that the lee filter tends to under smooth images and performs poorly when the original speckle noise image content is high. The Kuan filter performs best over a certain range of noise values. Finally, we note that the new technique shows improved S/MSE values.

6.8 Summary

This section illustrated the superiority of the proposed wavelet filter, showcasing various images and numerical analysis. In the next section, we investigate the application of the noise reduction algorithm to improve motion estimation techniques in ultrasound video images.

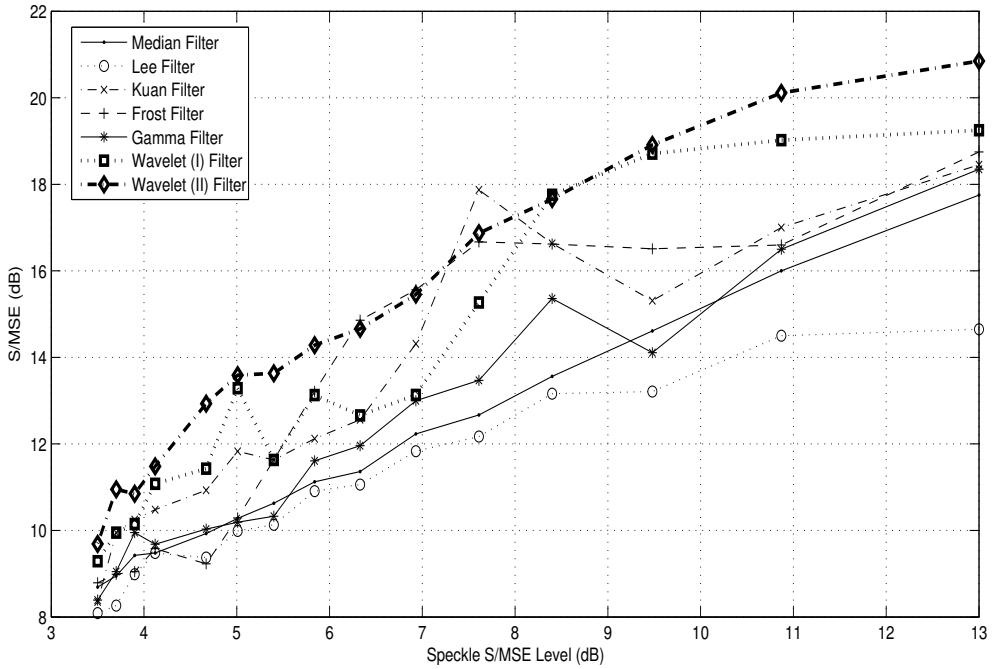

Figure 6.14: Comparison between the proposed scheme (with soft thresholding) against various standard filters

Chapter 7

Applications in Cardiac Motion Estimation

The heart has a vital function in the body as malfunctions may have fatal consequences. Coronary artery disease remains one of the leading causes of death in developed nations. Real time analysis of heart dynamics can aid in clinical evaluations and diagnosis of cardiac diseases. Cardiologists believe that analysis of the motions of the heart, especially the left ventricle (LV), can give precise information about the health of the myocardium. Left ventricular motion and dynamic variation in the thickness of the myocardium provide clinicians with useful information about functional abnormalities.

While advances in medical imaging has provided much insight into visualizing internal structures, identifying organ motion still represents an open research problem. In estimating motion, the 2D motion field is defined by the projection of the 3D motion on the 2D image plane. Optical flow, defined as to the spatiotemporal variation of intensity, is ideally assumed to correspond to 2D motion. However, this

assumption is poor for ultrasound images due to the presence of speckle noise and suboptimal image formation conditions. While some challenges are inherit to the image formation process; others problems are inherit to the imaging modality. For ultrasound imaging, the presence of speckle noise degrades image quality and the ability to analyze relevant information. Furthermore, changes between successive frames in the digitized image sequence may be caused by either the relative motion between the organ and the imaging device, the noise in the electronics, or the organ movements themselves.

Echocardiography represents the most widely adapted modality to assess cardiac functions due to its non-invasive nature. Recent developments in ultrasound technology have also led to real-time image acquisition and processing of cardiac functions. Unfortunately, one important aspect of cardiac assessment not using echocardiographic measurements is estimating the elasticity and contractility of the myocardium. This is currently determined from cardiac motion using tagged MR images. One application of the above mentioned denoising technique is in applying the results in the development of a novel complex value-based multiresolution cardiac motion estimation algorithm using 2D echocardiographic images.

Alongside improvements to imaging hardware, the proposed algorithm mitigates several issues in medical ultrasound motion estimation. The main hypothesis is that the probe and patient do not move (breathhold imaging) while a sequence of N images (or frames) is acquired by the operator; such a sequence must cover the cardiac cycle entirely. A speckle reduction filter is applied to the image sequence prior to applying motion estimation (ME) algorithms in an attempt to identify motion vectors independent of changes in the image formation process. Further, the proposed algorithm takes advantage of the newly developed ETR speckle reduction filter to integrate the speckle reduction and motion estimation steps, further

reducing computation load.

Most approaches are based on deformable and mechanical modeling, requiring an initial segmentation step. Contour formulation is difficult and computationally intensive due to the speckle noise in ultrasound and the complexity of cardiac structures. The proposed algorithm computes a dense cardiac displacement field calculated directly from the speckle-noise-filtered ultrasound images, using the directional selectivity and shift-invariant properties of the multiresolution dual-tree complex wavelet transform (DT CWT) for improved computational complexity. The dense motion vector field can be found through a vector field interpolating process. Results show improved computation efficiency. Further simulations are required to determine accuracy compared to other standard hierarchical algorithm.

7.1 Review of Medical Principles

Even with limited access to the heart, it is possible to direct an ultrasound beam at most cardiac structures. [10] Standardize echocardiography examinations are based on three orthogonal planes, as shown in figure 7.1. The long-axis plane sections the heart starting from the aortic root and ending at the left ventricular apex. The plane includes the aortic and mitral valves. The long-axis is almost perpendicular to the plane containing the sternum and runs approximately from the right shoulder to the left kidney. The short axis runs approximately parallel to the atrioventricular junction plane. The short axis is at right angles to the plane of the sternum and runs from the left midclavicle to the right hip. As its name implies, the four-chamber plane includes parts of each of the four cardiac chambers, situated at right angles to both the long and short axes. It runs from the apex to the base of the heart and is approximately perpendicular to both the posterior interventricular septum and

the interatrial septum. On the surface, it is parallel to the plane of the sternum, and includes both the apex and the right shoulder [7].

The types of heart wall motion abnormalities are: decreased extent of inward motion (hypokinesis); no systolic inward motion (akinesis); and outward systolic bulging (dyskinesis) [41]. In general, most cardiac abnormalities can be detected by analysis of wall motion frame by frame in one of the three standard cardiac planes. Digitizing and automating these techniques can provide clinicians with useful tools in diagnosis. For example, generalized wall motion abnormalities occurring in dilated cardiomyopathy and end-stage valvular heart disease maybe identified using digital algorithms. Regional wall motion abnormalities occurring in ischaemic heart disease (whereby the wall motion is delayed) may also be identified using automated analysis.

Tracking the non rigid motions of the heart has been traditionally approached by one of three methods. The first method physically implants track markers into the LV wall and detects motion using MR tagging techniques [42]. While MR tagging shows some success in motion estimation, this approach is invasive, requiring surgery to implant the markers. The second approach detects motion by the changes in the grey level values of every pixel in the image. This approach is based on extracting information about the cardiac wall from each diagnostic image and analyzing motion subsequently [43]. A set of boundaries for the heart is calculated initially using deformable modeling. Results are optimized using block matching techniques with an appropriate cost function and a composition flow field over the sequence is calculated [44]. This technique is error prone as speckle noise hinders the initial segmentation step. Recently, tissue velocities have been successfully analyzed by Doppler techniques [45]. However, Doppler echocardiography are highly angle dependent as they can only determine the velocity component towards the

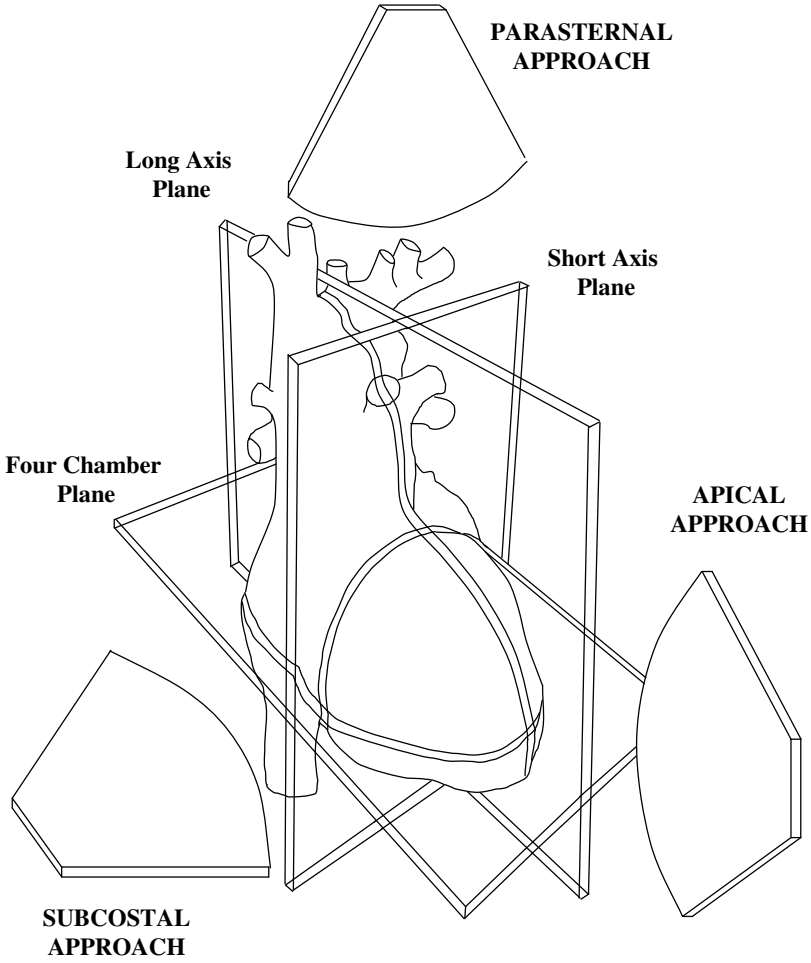

Figure 7.1: Standard Imaging Planes for Echocardiography [7]

transducer position. This paper is a variation of the second approach, calculating a dense motion field in echocardiographic sequences and addressing the difficulty of boundary estimation and heavy computational complexity which hinders motion estimation using contour segmentation.

7.2 Survey of Standard Motion Estimation Techniques

Motion can be defined in terms of either instantaneous velocity or displacement. Instantaneous velocity, $\vec{v}$, and displacement, $\vec{d}$, are related by a constant corresponding to the temporal sampling interval, Δt, due to the discrete nature of image sequences over time. Except in the case where parameter estimation models are used, these terms are interchangeable. This paper will define motion vectors in terms of displacement.

Motion estimation is an active area of research for video coding and computer vision. Motion estimation is related to the projection of an object's 3D velocity on the image plane. A dense estimated motion field yields the motion vectors on a regular grid of the image. A number of very different motion estimation algorithms have been proposed in literature and can be divided into four groups: block matching techniques, gradient techniques, pel-recursive techniques, and frequency-domain techniques.

Block matching techniques are based on minimizing a cost function. The theoretical model usually assumes that an image is composed of rigid objects in translational motion. This algorithm partitions images into blocks with the same displacement vector assigned to all pixels within a block. Finding an absolute minimum for

the matching criterion can only be guaranteed by performing an exhaustive search of a series of discrete candidate displacements within a maximum displacement range. Fast search techniques [11] and adaptive multigrid techniques [46] have been recently investigated. Relaxing the translational constraint to account for affine transformations have also been investigated [47]. However, the block matching technique is computational complex and accurate estimation is difficult due to block artifacts and poor motion compensated prediction along moving edges.

Gradient based approaches for motion estimation (Optical Flow) refer to those techniques that estimate the motion of an image sequence based on local derivatives in the image intensity. Gradient techniques resolve the video sequence into dense motion fields by assuming that image luminance is invariant along motion trajectories. By a Taylor series expansion of the image intensity and neglecting the higher order terms, an optical flow constraint equation is defined. In addition to the spatio-temporal constraint equation, an additional constraint is introduced to regularize the ill-posed aperture problem to solve the optical flow as the first constraint can only define the component parallel to the intensity gradient. One algorithm introduced by Horn-Schunck exploits a smoothness constraint to minimize the square of the optical flow gradient magnitude [48]. In this algorithm, the minimization is solved using variational calculus by an iterative Gauss-Seidel procedure. Recently, hierarchical schemes [49], and local uniformity constraints [47] have been proposed. Unfortunately, gradient techniques suffer from accuracy as the smoothness constraint leads to an increased energy of the prediction error, particularly on moving object boundaries.

Pel-recursive techniques can be considered as a subset of the gradient techniques as it recursively minimizes the prediction error (spatio-temporal constraint) or the difference in displacement between successive frames. A pel represents the smallest

discrete component in an image. Netravali-Robbins developed the first pel-recursive algorithm by iteratively minimizing the difference in displacement using the steepest decent technique [50]. Recently, multiple frames model-based approach [47] and multiple mask regularization techniques [12] have been proposed. Unfortunately, the Pel-recursive algorithms suffer from several drawbacks. First, the error function contains many local minima in general and the iterative procedure may converge to a local minimum rather than the global minimum. Secondly, large displacement and discontinuities in motion fields are not handled efficiently due to noise sensitivity.

Frequency-domain techniques are based on the relationship between transformed coefficients of shifted images and have only recently become popularized. One class of spectral algorithms are based on the notion that if a sequence of images contains a linearly moving pattern, then the energy of the Fourier transform (FT) of this function will be concentrated along a plane through the origin whose orientation is related to the velocity of the moving pattern [51]. So by computing the transform, a plane with strong energy concentration can be used to estimate the desired velocity. The existence of multiple superimposed motions will be manifested in the spectrum simply as energy concentration along more than one plane through the origin. Another class of algorithms involves expanding each frame into a multiresolutional pyramid structure and successively applying pel-recursion or gradient schemes to estimate the motion. The wavelet transform was designed to improve spectral techniques as it allows for spatial and frequency resolution. The motion vector is estimated at the coarsest resolution and then manipulated as finer resolution coefficients are considered. Fleet and Jepson [52] proved that phase adheres more closely to the local translation model than image intensity under affine deformations. The proposed algorithm uses a coarse-to-fine phased based complex wavelet transform to estimate motion. The phase-correlation method measures the

motion directly from the phase correlation map, giving accurate and robust motion vector estimates, and a low entropy motion field.

7.3 Enhanced Motion Estimation using Wavelet Speckle Noise Filtering

Using the standard block motion estimator and the wavelet denoising algorithm, the following motion field was detected as shown in figure 7.2. Note that without noise reduction, the motion fields could not be found. In the image, the motion of the blood and wall can be determined.

7.4 Summary

This chapter investigated a potential application of the proposed Elliptical Thresholding and Rotating noise reduction algorithm. The next chapter summarizes the contributions of this thesis and suggests future research direction.

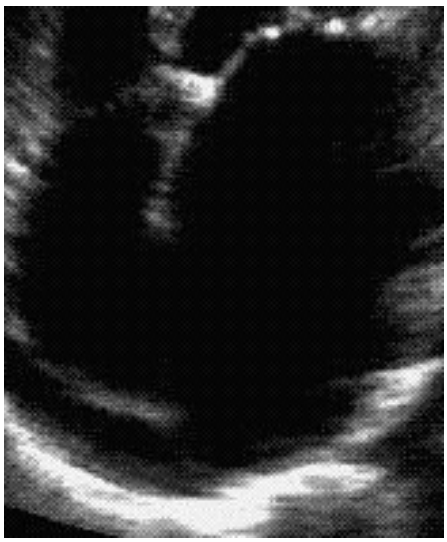

(a) Frame 1

(b) Frame 2

(c) Motion Detected between Frame 1 and Frame 2

Figure 7.2: Motion Fields of Cardiac Ultrasound Image

Chapter 8

Conclusions and Future Research

A comparative study between wavelet shrinkage technique and standard speckle filters has been presented. The following filters were tested: Median, the Lee, the Kuan, the Enhanced Frost, the Gamma MAP, and the type I and type II proposed wavelet filters. There are two advantages to using the ETR algorithm over the standard filter strategies. Firstly, the different parameters allow for adjustment based on the spectral content of the image to smooth out noise and retain edges. Secondly, the filter further decorrelate the relationship between noise and signal through elliptical rotations to restore the original scene.

This report also studied the impact of correlation properties and the first order statistical properties of speckle in the complex wavelet domain. It was shown using an ultrasound image model, that the correlation has an effect on the wavelet decomposition up the speckle grains. As multiplicative noise increases the wavelet coefficients, the wavelet coefficients will be different with different reflectivity. The paper further modelled the complex wavelet coefficients in the SD and DT CWT domain. Using ML estimators, a computationally efficient and moderately accurate

model for the SD CWT wavelet coefficients were found. It was found that approximation using a Rayleigh distribution for the amplitude and a mixed Gaussian (with 2 individual Gaussian distributions) were adequate to model the underlying wavelet coefficient distributions. Similar results were found for the log transformed model although further investigation into the nature of the RMS error value deviations are required.

8.1 Summary of Contributions

The proposed algorithm performs rotational wavelet shrinkage with the following features:

- independent thresholding is performed in the 3 wavelet sectors
- each wavelet block is assumed to follow a bi-normal distribution
- thresholding is done with respect to the principal coordinate axes
- thresholding is angle-dependent and follows the distribution eccentricity
- recovery the correct wavelet coefficient distribution orientation of the hidden signal.

The method significantly reduces the speckle while preserving the resolution and sharp features in the original image. In most circumstances, it gives better visual quality than the median and geometric filters. The new technique has the advantages of robust parameter selection, speed of computation and preservation of texture and organ surfaces. The new technique has a large potential in

real-time ultrasound imaging enhancement and in assisting automated segmentation/calculation techniques.

The orientation of the principal coordinate axes, with respect to the (x; y) coordinates is a characteristic of the image and of the chosen wavelet. Numerical experiments have shown that the orientations on the first decomposition levels are affected by the noise content.

We also gave measures of the variation of the S/MSE ratio over a wide range of filter parameters in order to get information on the optimal application range of the filter in practical situations.

A comparison of the speckle reduction properties of various filters were also analyzed using the S/MSE ratios and the ENL factor for clinical real world images. Simulations suggest the proposed denoising technique offers superior visual quality, though its signal-to-mean-square-error ratio (S/MSE) is numerically comparable to adaptive Frost filtering.

8.2 Future Research Directions

In this thesis, we have applied a nonlinear wavelet algorithm to remove speckle noise. The proposed wavelet filter is superior to the Wiener filter and other stand filters because of its edge and feature-sensitive selectivity in passing certain high-frequency data. The following improvements can be made to the denoise algorithm:

- The HVS models for image assessment should be used as an assessment strategy for the algorithm presented.
- Opinions from medical experts regarding the validity of the resulting images should also be addressed.

In the statistical modelling the DT CWT wavelet coefficients, results were not as promising. Only the amplitude in the intensity domain seem to provide acceptable results. Further investigation of the DT CWT case is necessary before further conclusions can be drawn. Expanding the modeling dataset to include a larger number of images will also lend greater credibility to the analysis. To improve the results from the analysis, one can attempt to increase the complexity of the Gaussian mixture model. Currently, the application of the dual mixed Gaussian model does not seem to fit the complex domain coefficients perfectly as the PDF peaks sharply and have extensive tails similar to the DWT case [40]. Application of a mixed Gaussian model where each peak is modelled by two Gaussian models of different variance superimposed may improve the coefficient modelling. This approach offers an increase mathematical complexity but greater support for the sparse nature of wavelet coefficients. To classify the coefficients, one solution proposed by [8] involves the use of a hidden Markov model with one binary state. This model will further optimize the division between the two superimposed models based on image statistics. The EM algorithm can be applied for estimation of multivariant Gaussian distribution parameters.

This thesis also looked into standard motion estimators on echocardiographic images and the impact of noise reduction in enhancing the detection of motion fields and boundaries. Preliminary analysis of motion estimators shows promising results. To further exploit the wavelet domain representation, a top down/bottom up motion estimator based on complex decomposition should be investigated.

Bibliography

[1] M. E. Anderson and G. E. Trahey. (2000, Apr.) A seminar on k-space applied to medical ultrasound. [Online]. Available: http://dukemil.egr.duke.edu/Ultrasound/k-space/

[2] J. A. Jensen, *Estimation of Blood Velocity Using Ultrasound*. New York, New York: Cambridge University Press, 1996.

[3] P. N. T. Wells, *Advances in Ultrasound Techniques and Instrumentation*. New York: Churchill Livingstone, 1993.

[4] J. U. Quistgaard, "Signal acquisition and processing in medical diagnostic ultrasound," *IEEE Signal Processing Magazine*, pp. 67–74, Jan. 1997.

[5] J. A. Zagzebski, *Essentials of Ultrasound Physics*. St. Louis, Missouri: Mosby, 1996.

[6] P. N. T. Wells, "Absorption and dispersion of ultrasound in biological tissue," *Ultrasound in Medicine and Biology*, vol. 1, 1975.

[7] H. Feigenbaum, *Echocardiography*, 5th ed. Philadelphia, Pennsylvania: Lea and Febiger, 1994.

[8] L. H. Xie, Pierce, and F. T. Ulaby, "Sar speckle reduction using wavelet denoising and markov random field modeling," *IEEE Trans. Geosci. Remote Sensing*, vol. 40, no. 10, Oct. 2002.

[9] A. F. Abdelnour and I. W. Selesnick, "Nearly symmetric orthogonal wavelet bases," in *Proc. IEEE on IEEE Int. Conf. Acoust., Speech Signal Processing (ICASSP)'2001*, May 2001.

[10] C. Behrenbruch, M. Brady, G. Jacob, and J. Noble, "Adaptive multiresolution detection of the epicardial wall in 2d cardiac ultrasound," in *Proc. on Medical Image Understanding and Analysis*, 1999, pp. 98–93.

[11] A. Chimienti, C. Ferraris, and D. Pau, "A complexity-bounded motion estimation algorithm," vol. 11, no. 4, pp. 387–392, 2002.

[12] S. N. Efstratiadis and A. K. Katsaggelos, "An adaptive regularized recursive displacement estimation algorithm," vol. 2, pp. 341–352, 1993.

[13] J. Goodman, "Some fundamental properties of speckle," *Journal of Optical Society*, vol. 66, no. 11, pp. 1145–1150, 1976.

[14] J. S. Lee, "Refined filtering of image noise using local statistics," *Journal of Computer Graphic and Image Processing*, vol. 15, pp. 380–389, 1981.

[15] Z. Shi and K. B. Fung, "A comparison of digital speckle filters," in *Proc. IEEE on IGARSS ('94)*, vol. 4, Aug. 1994, pp. 2129–2133.

[16] D. Kuan, A. Sawchuk, T. Strand, and P. Chavel, "Adaptive noise smoothing filter for images with signal-dependent noise," vol. 7, no. 2, Mar. 1985.

[17] ——, "Adaptive restoration of images with speckle," vol. 35, no. 3, Mar. 1987.

[18] V. Frost, J. Stiles, K. Shanmugan, and J. Holtzman, "A model for radar images and its application to adaptive digital filtering of multiplicative noise," vol. 4, no. 2, Mar. 1982.

[19] A. Lopes, R. Touzi, and E. Nezry, "Adaptive speckle filters and scene heterogeneity," vol. 28, no. 6, Nov. 1990.

[20] S. G. Mallat, *A Wavelet Tour of Signal Processing*, 2nd ed. Burlington, MA: Academic Press, 1999.

[21] I. Daubechies, *Ten Lectures on Wavelets*. Philadelphia, Pennsylvania: Society for Industrial and Applied Mathematics, 1992.

[22] J. L. Donoho, "De-noising by soft-thresholding," vol. 41, no. 3, pp. 613–627, May 1995.

[23] S. G. Mallat, "A theory for multiresolution signal decomposition: the wavelet representation," vol. 11, no. 7, pp. 674–693, July 1989.

[24] ——, "Multifrequency channel decompositions of images and wavelet models," in *Proc. IEEE on Acoustics, Speech, and Signal ('89)*, vol. 37, no. 12, Dec. 1989, pp. 2091–2110.

[25] A. Achim, A. Bezerianos, and P. Tsakalides, "Ultrasound image denoising via maximum a posteriori estimation of wavelet coefficients," in *Proc. IEEE on Engineering in Medicine and Biology ('01)*, vol. 3, Oct. 2001, pp. 2553–2556.

[26] A. Pizurica, W. Philips, I. Lemahieu, and M. Acheroy, "A versatile wavelet domain noise filtration technique for medical imaging," vol. 22, no. 3, pp. 323–331, Mar. 2003.

[27] L. Gagnon, "Wavelet filtering of speckle noise - some numerical results," in *Proc. on the Conference Vision Interface ('99)*, Trois-Rivieres, Canada, May 1999, pp. 1–8.

[28] L. Gagnon and F. D. Smaili, "Speckle filtering of sar images - a comparative study between complex-wavelet-based and standard filters," in *Proc. of the Society of Optical Engineering*, vol. 3169, 1997, pp. 81–91.

[29] J. M. Lina, "Complex daubechies wavelets: Filters design and applications," in *Proc. on ISACC CRM-2449 (ISACC'97)*, June 1997, pp. 1–18.

[30] R. Coifman and D. Donoho, *Lecture Notes in Statistics and Wavelets: Translation Invariant De-noising.* New York: Springer-Verlag, 1995, pp. 125–150.

[31] N. Kingsbury, "Complex wavelets for shift invariant analysis and filtering of signals," *Journal of Applied and Computational Harmonic Analysis*, vol. 10, pp. 234–253, 2001.

[32] ——, "Design of q-shift complex wavelets for image processing using frequency domain energy minimization," in *Proc. IEEE on Image Processing*, 2003.

[33] ——, "Shift invariant properties of the dual-tree complex wavelet transform," in *Proc. IEEE on Acoustics, Speech, and Signal Processing*, 1999.

[34] J. Neumann and G. Steidl, *Dual-Tree Complex Wavelet Transform in the Frequency Domain and an Application to Signal Classification*, 1st ed. U. Mannheim, 2003.

[35] M. Simard *et al.*, "Analysis of speckle noise contribution on wavelet decomposition of sar images," vol. 36, no. 6, Nov. 1998.

[36] D. Wei, M. Lang, H. Guo, J. E. Odegard, and C. S. Burrus, "Quantization noise reduction using wavelet thresholding for various coding schemes," in *SPIE Math. Imaging: Wavelet Applications in Signal and Image Processing (2569)*, July 1995.

[37] A. P. Dempster, N. M. Laird, , and D. B. Rubin, "Maximum likelihood from incomplete data via the em algorithm," *Journal of Statistics*, vol. 29, no. 1, pp. 1–28, 1977.

[38] D. L. Donoho and I. M. Johnstone, "Threshold selection for wavelet shrinkage of noisy data," in *Proc. IEEE on Engineering in Medicine and Biology*, vol. 1, Nov. 1994, pp. A24–A25.

[39] L. Gagnon and F. D. Smaili, "Speckle noise reduction of airborne sar images with symmetric daubechies wavelets," in *Proc. of the Society of Optical Engineering*, vol. 2759, 1996, p. 1424.

[40] A. Achim, A. Bezerianos, and P. Tsakalides, "Wavelet-based ultrasound image denoising using an alpha-stable prior probability model," in *Proc. IEEE on Image Processing ('01)*, vol. 2, Oct. 2001, pp. 221–224.

[41] M. Suhling, M. Arigovindan, C. Jansen, P. Hunziker, and M. Unser, "Myocardial motion analysis and visualization from echocardiograms," in *Proc. SPIE on Medical Imaging*, vol. 5032, no. 1, 2003, pp. 306–313.

[42] N. Ingels, G. Daughters, E. Stinson, and E. Alderman, "Measurement of midwall myocardial dynamics in intact man by radiography of surgically implanted markers," *Circ.*, vol. 52, pp. 859–867, 1975.

[43] J. C. I. McEachen and J. S. Duncan, "Shape-based tracking of the left ventricular wall motion," *IEEE Trans. Med. Imag.*, vol. 16, no. 3, pp. 270–283, 1997.

[44] M. J. Ledesma-Carbayo *et al.*, "Cardiac ultrasound motion detection by elastic registration exploiting temporal coherence," in *Proc. IEEE on Biomedical Imaging*, vol. 2, 2002, pp. 585–588.

[45] K. V. Ramnarine *et al.*, "Tissue doppler imaging of carotid plaque wall motion: a pilot study," *Cardiovascular Ultrasound*, vol. 1, no. 17, 2003.

[46] E. Memin and P. Perez, "Hierarchical estimation and segmentation of dense motion fields," *International Journal of Computer Vision*, vol. 46, no. 2, pp. 129–155, 2002.

[47] F. Dufaux and F. Moscheni, "Motion estimation techniques for digital tv: A review and a new contribution," in *Proc. IEEE on Engineering in Medicine and Biology*, vol. 83, no. 6, 1995, pp. 858–876.

[48] B. K. P. Horn and B. G. Schunck, "Determining optical flow," *Artificial Intelligence*, vol. 17, pp. 185–203, 1981.

[49] N. Haddadi and C. Kuo, "Multiple bit-rate video compression via progressive motion field coding," in *Proc. of the Society of Optical Engineering in Image and Video Compression*, vol. 2186, 1994, pp. 233–244.

[50] A. Netravali and J. D. Robbins, "Motion compensated television coding part i," *Journal Bell System Technology*, vol. 58, no. 3, pp. 629–668, 1979.

[51] J. F. Watkinson, *The Engineer's Guide to Motion Compensation*. Hampshire: Snell and Wilcox, 1994.

[52] D. J. Fleet and A. D. Jepson, "Computation of component image velocity from local phase information," *International Journal of Computation and Vision*, vol. 5, pp. 77–104, 1990.

Appendix A

MATLAB GUI for Speckle Reduction Algorithm

Figure A.1 shows user interface to the speckle noise algorithm implemented. Note that thresholds can be varied and instant S/MSE values for be identified quickly.

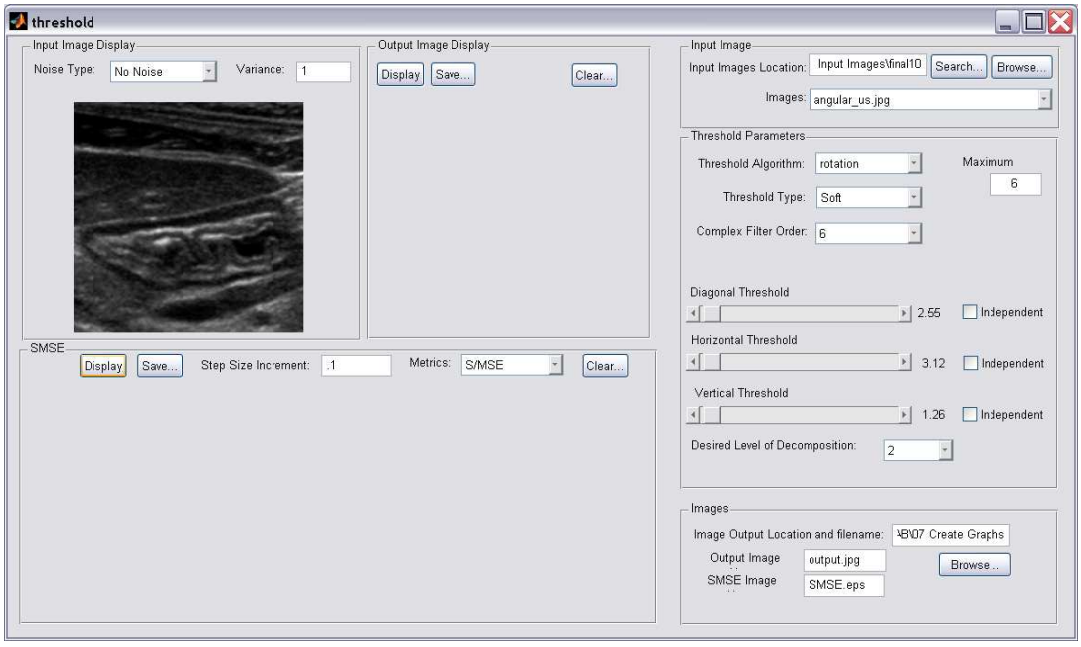

Figure A.1: Proposed Wavelet GUI used for speckle noise reduction

The top left corner shows the input image while in the right handed side, the speckle reduced image is shown. The far right handed side allows the user to change the parameters of the ETR algorithm. Finally, the bottom section shows the graphs (S/MSE vs noise level) generated from mass image simulation.